



**Anisotropic molecular photoemission dynamics: Interpreting and accounting for the nuclear motion**

Antoine Desrier, Morgan Berkane, Camille Lévêque , Richard Taïeb, and Jérémie Caillat <sup>\*</sup>  
*Sorbonne Université, CNRS, Laboratoire de Chimie Physique-Matière et Rayonnement, LCPMR, F-75005 Paris, France*

 (Received 12 February 2024; accepted 23 April 2024; published 21 May 2024)

We investigate how vibration affects molecular photoemission dynamics, through simulations on two-dimensional asymmetric model molecules including the electronic and nuclear motions in a fully correlated way. We show that a slight anisotropy in the electron-ion momentum sharing is sufficient to prevent one from unambiguously characterizing the vibrationally averaged photoemission dynamics in terms of stereo Wigner delays. We further show that vibrational resolution can be retrieved in fixed-nuclei simulations, using effective molecular conformations that are specific to each vibrational channel. The optimal internuclear distances found empirically in one-photon processes can be identified *a priori* using simple physical arguments. They also turn out to be efficient to simulate vibrationally resolved interferometric measurements and to account for interchannel coherences in broadband one-photon ionization.

DOI: [10.1103/PhysRevA.109.053106](https://doi.org/10.1103/PhysRevA.109.053106)

**I. INTRODUCTION**

From its early emergence as an applied branch of attosecond sciences to its most recent and ongoing developments, attochemistry offers and envisions unprecedented ways of exploring fundamental dynamics occurring in molecules on their natural timescale [1–7]. In the broader perspective of attosecond time-resolved spectroscopies, photoemission takes a singular role, either as a characterization tool [8,9] or as the probed process itself [10–12].

Revisiting a process as essential as molecular photoemission in the time domain is made possible only through intertwined long-term interactions between theory and experiments that tackle and exploit the complexities and richness specific to molecular systems both in the conception and in the interpretation of simulations or measurements. It was pioneered by investigating experimentally the intricate dynamics of resonant ionization in N<sub>2</sub> with vibrational resolution [13], using the “reconstruction of attosecond beating by interference of two-photon transitions” (RABBIT) technique [8,14]. The interpretation of the measured channel-selective RABBIT phase in terms of transition delays was subsequently clarified by means of simulations on low-dimensional model molecules [15,16]. The experimental results were furthermore reproduced and expanded recently in elaborate simulations aiming at quantitative agreement [17]. The anisotropy of ionization dynamics, which is another essential feature of molecular photoemission, was considered first in simulations of attosecond streaking measurements [9,18] on a model CO molecule [19] and then explored experimentally, also on CO, using RABBIT [20]. Further experimental and theoretical investigations addressing anisotropy have since been reported on systems of increasing complexities [21–26] (see also [27] and references therein).

The imprints of nuclear motion on photoemission dynamics in polyatomic molecules is the subject of an

increasing number of theoretical and experimental investigations. Among the most recent studies, the authors of Ref. [28] investigated theoretically how nuclear motion affects photoelectron spectra in the context of RABBIT measurements. In this context, they established an expression of molecular RABBIT spectra in terms of a convolution between a nuclear autocorrelation function and two-photon electronic transition matrix elements, following an approach initially derived to simulate molecular streaking [29]. In [30] the imprints of nuclear motion on attosecond photoemission delays was investigated experimentally on the methane molecule and its deuterated counterpart, using RABBIT and advanced theoretical support. The authors found no significant isotopic effect, but found an approximately 20-as difference between dissociative and nondissociative channels. A closely related study on the same polyatomic molecules further highlighted how nuclear motion impacts the coherence of the photoemission process [31], which is an essential issue for most of the interferometric attosecond-resolved pump-probe schemes.

Nonetheless, investigations on smaller (diatomic) benchmark molecules [32–44] remain of great importance to gradually and comprehensively explore the interplay of the molecular degrees of freedom from a time-dependent perspective. On the theory side, simulations on simple models with limited degrees of freedom [45] are essential to guide and interpret experiments and elaborate simulations in terms of intuitive pictures and practical notions.

In the present article we investigate numerically how vibration imprints the attosecond dynamics of anisotropic molecular photoemission even when the vibronic couplings are minimal, notably far from any vibronic resonance.<sup>1</sup> Our study is based on low-dimensional model molecules

<sup>1</sup>We consider the present work a companion paper to Ref. [27], which focuses on the definition and RABBIT measurements of anisotropic molecular photoemission delays, regardless of the nuclear motion.

\*jeremie.caillat@sorbonne-universite.fr

allowing for extensive numerically exact simulations. The objectives are twofold: (i) to study the interplay of molecular asymmetry and nuclear motion on attosecond time-resolved photoemission and (ii) to identify a way to account for the vibrational resolution in standard theoretical approaches with fixed nuclei, keeping in mind that only the latter can be routinely applied to the simulations of more realistic models.

The paper is organized as follows. Section II presents the model molecules and the overall methodology followed in our study. In Sec. III we benchmark the signatures of molecular asymmetry on one-photon ionization dynamics with a model displaying no effective nuclear motion during photoemission. This model partly reproduces and expands the results presented and discussed in [27]. In Sec. IV we consider photoemission occurring with sensible nuclear motion. We question the relevance of defining an orientation-resolved photoemission delay for the photoelectron wave packet averaged over the open vibrational channels. Then we consider vibrationally resolved photoemission dynamics and investigate the possibility to reproduce it in a fixed-nuclei approach. In Sec. IV C we address the capacities of the fixed-nuclei approach to reproduce coherent, vibrationally resolved photoemission beyond the context in which it was designed. A summary and conclusions are presented in Sec. V.

Unless stated otherwise, the quantities in equations are in atomic units throughout the paper.

## II. THEORETICAL TOOLBOX

### A. Model molecules

Our simulations were performed on single-active-electron diatomic model molecules including correlated electronic and internuclear motions, each in one dimension. They are similar to the ones used, e.g., in [15,46,47].

#### 1. Generic Hamiltonian

The generic field-free Hamiltonian of the model molecules reads

$$H_0 = \underbrace{-\frac{1}{2\mu} \frac{\partial^2}{\partial R^2} + V_{N-N}(R)}_{H_N} - \underbrace{\frac{1}{2} \frac{\partial^2}{\partial x^2} + V_{N-e}(x, R)}_{H_e}, \quad (1)$$

where the two coordinates  $x$  and  $R$  are the electron position and the internuclear distance, respectively,  $\mu$  is the reduced mass of the nuclei,  $V_{N-N}(R)$  is the interatomic potential in the absence of the active electron, and  $V_{N-e}(x, R)$  is the interaction potential between the active electron and the molecular ion. The interatomic potential  $V_{N-N}$  for each molecule is defined numerically on a discretized  $R$  grid, while the electron-nuclei potential  $V_{N-e}$  is defined as an asymmetric two-center soft Coulomb potential

$$V_{N-e}(x, R) = \sum_{j=1,2} -\frac{q_j}{\sqrt{(x - X_j)^2 + a(R)}}, \quad (2)$$

where

$$X_j = (-1)^j \frac{\mu}{M_j} R \quad (3)$$

are the positions of each nucleus ( $j = 1, 2$ ), of mass  $M_j$ , with respect to their center of mass. The  $V_{N-e}$  potential is adjustable through the effective charges  $q_j > 0$  (with the constraint  $q_1 + q_2 = 1$ ) and the screening parameter  $a(R) > 0$  defined numerically over the same  $R$  grid as  $V_{N-N}$ . One should note that  $V_{N-e}$  accounts not only for the asymmetry related to the electronegativity difference (through  $q_j$ ) but also for the mass asymmetry (through  $X_j$ ).

In practice, we adjusted  $V_{N-N}$  and  $V_{N-e}$  empirically [45] for the energies of the model molecule to match some desired energy curves within the Born-Oppenheimer (BO) approximation:  $V_{N-N}$  is directly the molecular ion energy curve, while the negative eigenenergies of  $H_e + V_{N-N}$  computed at each  $R$  [see the partition of  $H_0$  in Eq. (1)] provide the electronic ground and excited curves of the neutral. Within the BO framework, the ground-state energy  $\varepsilon_0(R)$  of the electronic Hamiltonian  $H_e$  is the opposite of the vertical ionization potential for each  $R$ ,

$$\tilde{E}_1(R) = -\varepsilon_0(R), \quad (4)$$

i.e., the energy gap between the ionic and the neutral ground-state curves.

### 2. Model parameters

We considered three model molecules, hereafter referred to as  $\mathcal{A}$ ,  $\mathcal{B}$ , and  $\mathcal{C}$  for simplicity. For each of them, the effective charges were set to  $q_1 = 0.33$  a.u. and  $q_2 = 0.67$  a.u. and the nuclei masses to  $M_1 = 20.53$  u and  $M_2 = 7.47$  u. The chosen masses are such that  $M_1 + M_2 = 28$  u, i.e., the mass of CO, a prototypical heteronuclear diatomic molecule on which orientation- and time-resolved photoemission simulations [19] and experiments [20] have already been performed. However, our models are only loosely based on CO, as we, among other liberties, increased the mass ratio  $M_2/M_1$  in order to emphasize the consequences of mass asymmetry on photoemission dynamics. The potentials were adjusted to obtain the BO curves displayed in Fig. 1. The three molecular systems share the same ground-state energy curve, which mimics the one of CO [48], with an equilibrium distance  $R_{\text{eq}} = 1.115$  Å.

In molecule  $\mathcal{A}$ , the ionic curve is a vertically shifted image of the ground state. In molecule  $\mathcal{B}$  ( $\mathcal{C}$ ), it is also a replica of the ground-state curve, translated towards smaller (larger) values of  $R$  with its minimum at 1.029 Å (1.201 Å). The energy shifts of the ionic curves were adjusted to achieve  $\tilde{E}_1(R_{\text{eq}}) \simeq 30$  eV for all molecules (29.81, 29.18, and 29.30 eV for molecules  $\mathcal{A}$ ,  $\mathcal{B}$ , and  $\mathcal{C}$ , respectively). As an illustration, the  $x$  dependence of the electron-core potential for molecule  $\mathcal{A}$  at the equilibrium distance  $R = R_{\text{eq}}$  can be found in Fig. 4(a). Due to the relative positions of these energy curves, photoionization takes place with no effective nuclear motion in molecule  $\mathcal{A}$ , while it initiates a bond contraction in molecule  $\mathcal{B}$  and an elongation in molecule  $\mathcal{C}$ .

### B. Methodology overview

We considered two different approaches for the simulations. The first one consists in simulating the complete vibronic dynamics of the model molecules. To this end, we performed numerically converged, vibronically correlated simulations based on solving the time-dependent Schrödinger

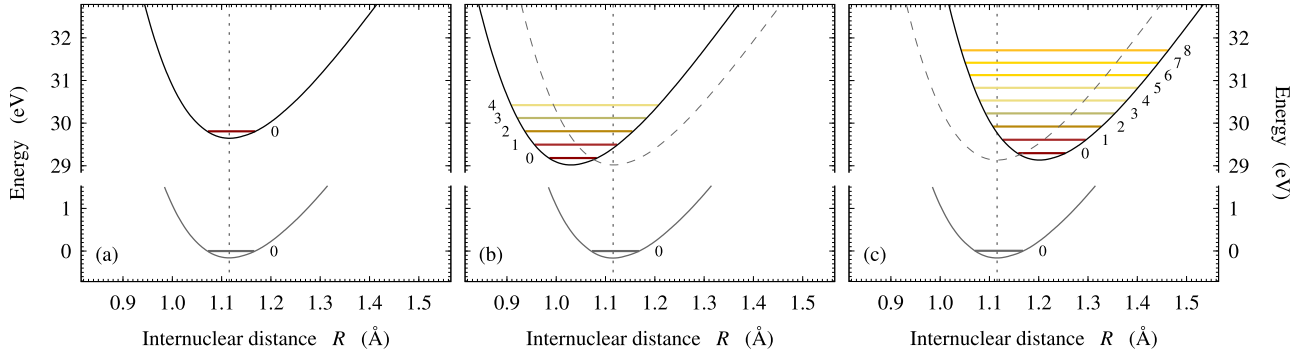


FIG. 1. Born-Oppenheimer energies of the model molecules (a)  $\mathcal{A}$ , (b)  $\mathcal{B}$ , and (c)  $\mathcal{C}$  designed for the simulations, as a function of the internuclear distance  $R$ . The energy scale here refers to the overall ground states of the neutral molecules. For each molecule, the gray solid and black solid curves correspond to the neutral and ionic electronic ground states, respectively. In (b) and (c) the gray dashed curve is an image of the neutral ground curve vertically shifted towards the ionization threshold, displayed for comparison. The vertical dotted lines indicate the equilibrium distance of the neutral molecule,  $R_{\text{eq}}$ . The vibrational levels  $v$  presenting a significant overlap with the ground state [ $|F(v)|^2 > 10^{-2}$ ; see Eq. (20) and Fig. 7] are indicated in the ionic curve of each molecule.

equation (TDSE). The second approach consists in adopting a standard simplified treatment with fixed nuclei, based on the BO approximation, where the photoemission dynamics is encoded in the continuum solutions of the electronic time-independent Schrödinger equation (TISE).

Our motivation is twofold. On the one hand, the complete vibronic simulations highlight the impact of vibronic couplings on the dynamics of molecular photoemission investigated with attosecond resolution. On the other hand, by comparing this exact dynamics with that obtained in the BO framework, we assess the relevance of fixed-nuclei approaches to investigate the molecular photoemission process (see, e.g., [19,23,49–52]), when these approaches are implemented with well-chosen molecular conformations. In all the simulations, the  $x$  origin was set *a priori* to coincide with the center of mass of the molecule, consistently with the definition of the  $V_{\text{N-e}}$  potential [see Eqs. (2) and (3)]. The central quantities used in this work to characterize anisotropic photoionization dynamics are orientation-resolved yields and stereo ionization delays, which can be computed indifferently in both approaches.

### 1. Complete simulations

The complete dynamics of the molecules was simulated by solving numerically the vibronic TDSE

$$i \frac{\partial \Phi(x, R, t)}{\partial t} = [H_0 + W(t)] \Phi(x, R, t). \quad (5)$$

Here  $\Phi(x, R, t)$  is the propagated vibronic wave function and  $W(t)$  represents the dipole interaction of the molecule with the ionizing pulse, implemented in the velocity gauge. The initial state is the ground vibronic state  $\Phi_0(x, R)$ , obtained by imaginary-time propagation, in all the simulations. The TDSE (5) was solved numerically using a split-operator propagation based on a grid representation of the  $x$  coordinate, combined with an expansion over a set of eigenvectors of  $H_{\text{N}}$  for the  $R$  coordinate, as detailed in [15,45]. The vector potentials of the ionizing pulses were assigned  $\sin^2$  temporal envelopes with central photon energies  $\omega_{\text{XUV}}$  corresponding to harmonics of a Ti:sapphire laser ( $\lambda_0 = 800$  nm and  $\hbar\omega_0 = 1.55$  eV) in the extreme ultraviolet (XUV). Case-specific pulse parameters are

indicated further in the text. Simulations on molecule  $\mathcal{A}$  were performed by expanding the wave function on a single vibrational state ( $v = 0$  is the only open channel). For molecules  $\mathcal{B}$  and  $\mathcal{C}$ , the results shown in this paper were obtained by including all vibrational channels up to  $v = 8$  and 17, respectively, which safely ensures convergence. The analysis of these complete time-dependent simulations are mostly based on the outgoing electron flux computed in the asymptotic  $x$  region, where the short-range components of  $V_{\text{N-e}}$  (including the vibronic couplings) vanish.

### 2. Simulations at fixed internuclear distances

In the BO framework, we treated one-photon ionization by analyzing electronic continuum wave functions computed at fixed internuclear distances. Among the solutions of the TISE

$$H_e \psi_\varepsilon(x) = \varepsilon \psi_\varepsilon(x) \quad (6)$$

in the degenerate continuum (at energies  $\varepsilon > 0$ ), we worked with the wave functions specifically selected by one-photon transitions starting from the ground state, hereafter referred to as selected continuum wave functions (SCWFs). These real-valued continuum wave functions are defined unambiguously, and their analysis and interpretation are independent of their definition and computation. The SCWF formalism was introduced in [53] and later used in [27,37]. Note that the electronic Hamiltonian  $H_e$  [as defined in Eq. (1)], its eigenfunctions  $\psi_\varepsilon(x)$ , and eigenvalues  $\varepsilon$  depend parametrically on the internuclear distance  $R$ , although it does not appear explicitly in Eq. (6) for the sake of readability. Within this framework, the dynamics of photoemission is encoded in the asymptotic features of the SCWF. More computational details are provided along with the presentation of the results.

## III. PHOTOEMISSION FROM MOLECULE $\mathcal{A}$ : SIGNATURES OF THE POTENTIAL ASYMMETRY

We present here the results obtained for molecule  $\mathcal{A}$ , which was designed to benchmark our methodological approach. We first detail the analysis of the time-dependent vibronic simulations and then verify that the latter are consistent with time-independent BO simulations at equilibrium distance.

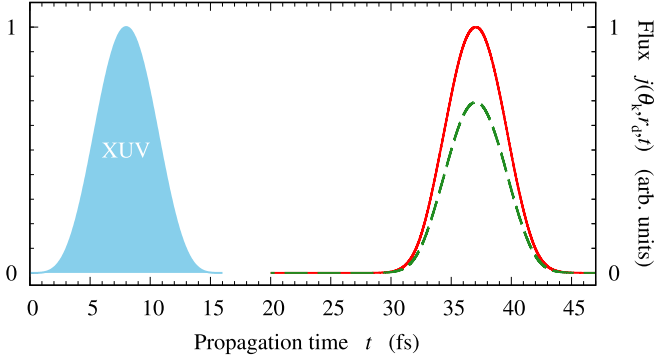


FIG. 2. Outgoing electron flux  $j(\theta_k, r_d, t)$  computed at  $r_d = 800$  a.u. on the left ( $\theta_k = 180^\circ$ , red solid curve) and right ( $\theta_k = 0^\circ$ , green dashed curve) sides of molecule  $\mathcal{A}$  ionized by an  $\omega_{\text{XUV}} = 35.67$  eV pulse, as a function of propagation time  $t$ . The flux is normalized to 1 at the overall maximum reached on the left side. The temporal envelope of the ionizing pulse is represented by the blue filled curve.

### A. Complete simulations

In these simulations, the XUV pulse intensities were set to  $10^{12}$  W/cm<sup>2</sup>, i.e., low enough to avoid any significant multi-photon process in one-color photoionization. The total durations of the  $\sin^2$  pulse envelopes were set to 16 fs, which corresponds to six fundamental periods ( $T_0 = 2\pi/\omega_0 = 2.67$  fs).

#### 1. Photoelectron flux

In the complete time-dependent simulations, we characterized the ionization dynamics through the outgoing photoelectron flux computed at a given detection distance  $r_d$  from the  $x$  origin, on either side of the molecule and averaged over  $R$ ,

$$j(\theta_k, r_d, t) = \cos \theta_k \text{Im} \int_0^\infty \Phi^*(r_d \cos \theta_k, R, t) \Phi'(r_d \cos \theta_k, R, t) dR, \quad (7)$$

where  $\Phi^*(x, R, t)$  is the complex conjugate of the vibronic wave function propagated according to Eq. (5) and  $\Phi'(x, R, t)$  is its derivative with respect to  $x$ . Here and throughout the paper,  $\theta_k$  represents the direction of photoemission, restricted to two discrete values:  $\theta_k = 0^\circ$  (emission towards the right,  $x > 0$ ) and  $180^\circ$  (towards the left,  $x < 0$ ).

As an illustration, Fig. 2 shows the flux computed at  $r_d = 800$  a.u. (423 Å) on the left and right sides of molecule  $\mathcal{A}$  ionized by a pulse of central frequency  $\omega_{\text{XUV}} = 23\omega_0 = 35.67$  eV. The flux profiles follow the ionizing pulse envelope (also shown), shifted by approximately 30 fs, which is consistent with the time needed for a (nearly) free electron with the energy  $\omega_{\text{XUV}} - \tilde{E}_1(R_{\text{eq}}) = 5.86$  eV to cover the distance  $r_d$ . The flux maximum approximately 1.5 times larger on the left side than on the right side is a clear signature of the photoemission anisotropy.

#### 2. Orientation-resolved yields and delays

We then computed the orientation-resolved yields

$$\mathcal{Y}(\theta_k) = \int j(\theta_k, r_d, t) dt \quad (8)$$

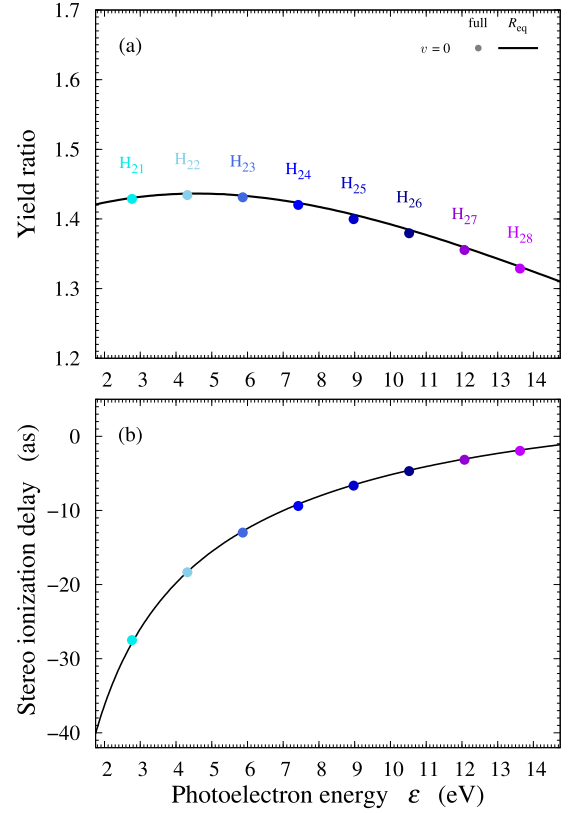


FIG. 3. Anisotropic photoemission from molecule  $\mathcal{A}$ . (a) Left-right ionization yield ratio computed in the fully correlated simulations and in the BO framework at  $R_{\text{eq}}$ ,  $\mathcal{R}$  [Eq. (9)] (line) and  $\tilde{\mathcal{R}}$  [Eq. (14)] (circles), respectively. (b) Stereo ionization delays computed in the fully correlated simulations and in the BO framework at  $R_{\text{eq}}$  and  $\Delta\tau$ , respectively [Eq. (11)] (line), and  $\Delta\tau_w$  [Eq. (16)] (circles). All data are plotted as a function of the photoelectron energy  $\varepsilon$ .

in a series of simulations with field frequencies corresponding to harmonics 21–28, i.e.,  $\omega_{\text{XUV}}$  ranging from 32.57 eV to 43.43 eV in steps of 1.55 eV. The corresponding yield ratio

$$\mathcal{R} = \frac{\mathcal{Y}(180^\circ)}{\mathcal{Y}(0^\circ)} \quad (9)$$

is displayed in Fig. 3(a) (colored circles) against the photoelectron energy  $\varepsilon$ . It evolves smoothly slightly above 1.4, indicating that photoemission is sensitive to the asymmetry of the ionic potential, with little variation over the energy range covered in the simulations.

To characterize the asymmetry of photoemission in the time domain, we used the average time of flight (TOF) [15,16,53] towards the detector in each direction as

$$\tau(\theta_k) = \frac{\int t j(\theta_k, r_d, t) dt}{\int j(\theta_k, r_d, t) dt}. \quad (10)$$

To further investigate the angular variations of the TOF computed as such, one must take into consideration the arbitrary origin  $x = 0$ , on either side of which the virtual detectors are located and which does not coincide with the average initial position of the electron. In the following, we will therefore characterize these angular variations by the origin-corrected



TOF difference

$$\Delta\tau = \tau(180^\circ) - \tau(0^\circ) - 2\frac{\langle x \rangle_0}{\sqrt{2\varepsilon}}, \quad (11)$$

where  $\langle x \rangle_0$  is the average initial electron position in the ground state of the molecule  $\Phi_0(x, R)$ ,

$$\langle x \rangle_0 = \langle \Phi_0 | x | \Phi_0 \rangle. \quad (12)$$

The role of the last term on the right-hand side of Eq. (11) is discussed in detail in the companion paper [27] in the context of time-independent approaches. Its justification identically holds for time-dependent simulations. It compensates for a spurious shift appearing when computing ionization delays with an arbitrary origin, while the photoelectron *on average* originates from  $\langle x \rangle_0$ . We verified numerically that including this term (after computing the TOFs) is equivalent to shifting the potential such that  $\langle x \rangle_0 = 0$  (prior to solving the TDSE). In the present simulations, as well as in molecules  $\mathcal{B}$  and  $\mathcal{C}$ ,  $\langle x \rangle_0 = -0.160 \text{ \AA}$ .

The stereo ionization delays  $\Delta\tau$  obtained for the considered set of XUV frequencies are plotted in Fig. 3(b). Starting from approximately  $-40$  as just below  $\varepsilon = 2 \text{ eV}$ , its magnitude decays smoothly while the photon energy increases, as could be expected in the absence of significantly structured continuum. Note that such attosecond delays cannot be resolved visually in Fig. 2, since they are extremely small compared to the temporal spread of the photoelectron wave packet at detection (approximately 16 fs, approximately the XUV pulse duration). They are nonetheless significant and we have ensured their numerical convergence. Among a series of standard numerical checks, we verified that the measured stereo delays  $\Delta\tau$  do not depend on the detection distance  $r_d$  (as long as it lies far enough from the ionic core), which is a fundamental property of the short-range scattering delays.

## B. Simulations at fixed internuclear distances

Here we consider the molecule  $\mathcal{A}$  at its equilibrium internuclear distance [see Fig. 4(a)]. It corresponds to the one-dimensional model molecule used for the numerical experiments presented and analyzed in [27].

### 1. Selected continuum wave function

The BO approach relies on the analysis of the electronic continuum wave functions  $\psi_\varepsilon(x)$  associated with the photoemission processes. We thus computed the SCWF of molecule  $\mathcal{A}$  by solving Eq. (6) over the same energy range as in the full time-dependent simulations, with a fixed internuclear distance set to  $R_{\text{eq}}$ .

The SCWF computed at the illustrative energy  $\varepsilon = 5.86 \text{ eV}$  (corresponding to  $\omega_{\text{XUV}} = 23\omega_0 = 35.67 \text{ eV}$ , as in Fig. 2) is shown in Fig. 4(b) (solid curve). The pseudoperiod of the oscillations on both sides is consistent with a kinetic energy asymptotically converging to  $5.86 \text{ eV}$ . Here the anisotropy of photoemission is clearly visible in the asymmetry of the *amplitudes* of the SCWF on either side of the molecule.

### 2. Orientation-resolved yields and delays

For each pulse frequency considered in the full-fledged approach, an alternative evaluation of the orientation-dependent

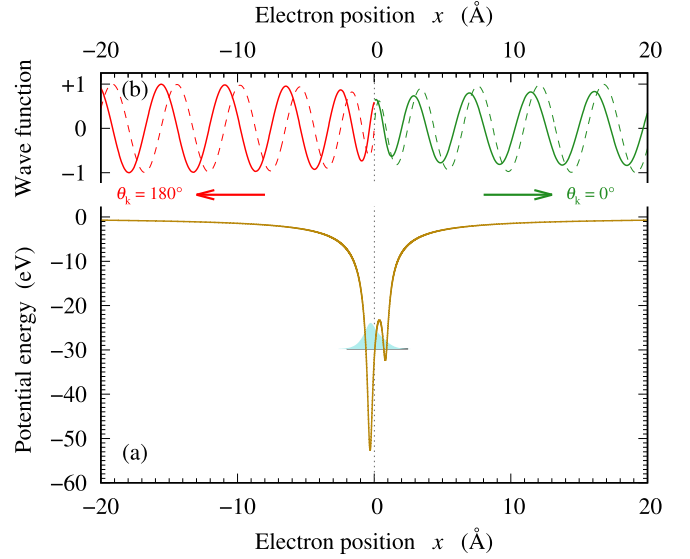


FIG. 4. Molecule  $\mathcal{A}$  in the BO framework (equilibrium internuclear distance). (a) Electron-nuclei potential  $V_{N-e}(x, R_{\text{eq}})$  as a function of the electron position  $x$  (dark yellow solid curve). The ground-state electronic wave function is also shown (light blue filled curve). (b) Electronic continuum wave function (solid curve) selected at the energy  $\varepsilon = 5.86 \text{ eV}$  by a one-photon transition from the electronic ground state. Odd-parity reference wave function (dashed curve) used to define and compute the orientation-dependent phase shifts. The displayed continuum wave functions are normalized such that their amplitudes asymptotically converge to 1 on the left-hand side of the molecule. In this figure, the left-right discrimination and the parity refer to the arbitrary  $x = 0$  origin (indicated by a vertical dotted line).

ionization yields is provided, up to a global factor, as

$$\tilde{\mathcal{Y}}(\theta_k) = |A(R_{\text{eq}}; \theta_k)|^2, \quad (13)$$

where  $A(R_{\text{eq}}; \theta_k)$  is the asymptotic amplitude of the SCWF computed with  $R = R_{\text{eq}}$ , at the average photoelectron energy, on each side of the molecule. We evaluated these amplitudes using Strömgren's normalization procedure (see [54] and references therein).

The corresponding yield ratio

$$\tilde{\mathcal{R}} = \frac{\tilde{\mathcal{Y}}(180^\circ)}{\tilde{\mathcal{Y}}(0^\circ)} \quad (14)$$

computed over the considered energy range is displayed as a solid line in Fig. 3(a). The perfect agreement with the ratio  $\mathcal{R}$  computed in the vibronic time-dependent simulations [Eq. (9)] constitutes the first numerical validation of our comparative approach.

From the time domain perspective, we analyzed the SCWF in terms of orientation-resolved Wigner delays [55], as detailed in [27]. Briefly, the Wigner delay is defined as the spectral derivative

$$\tau_w(\theta_k) = \frac{\partial \eta(\theta_k)}{\partial \varepsilon} \quad (15)$$

of the asymptotic phase shifts of the SCWF computed on each side of the model molecule, with respect to an arbitrary intermediate reference (here, radial Coulomb  $s$  waves centered

at  $x = 0$ ). As explained in [27], and consistently with the complete vibronic simulations, we characterized the angular variations of the photoemission dynamics in the BO framework through the origin-corrected stereo Wigner delay

$$\Delta\tau_w = \tau_w(180^\circ) - \tau_w(0^\circ) - 2\frac{\langle x \rangle_0}{\sqrt{2\varepsilon}}. \quad (16)$$

Since the exact ground state of the molecule is accurately modeled by its BO counterpart, the value of the initial average position  $\langle x \rangle_0$  is the same here as in the complete simulations. The stereo Wigner delays computed in the considered energy range, already shown in Fig. 3 of [27], are reported in Fig. 3(b) (solid line). They agree perfectly with the stereo delays computed in the complete time-dependent simulations.

Apart from benchmarking our comparative approach, the results obtained with molecule  $\mathcal{A}$  reveal the signatures of the left-right electronegativity asymmetry of the molecule on the photoelectron dynamics. The perfect agreement observed in Fig. 3 between the complete and the fixed-nuclei approach comes as no surprise since (i) the equivalence between the time-dependent and time-independent approaches has already been put forward by Wigner when interpreting in the time domain the group delay associated with a scattering phase shift [55] and (ii) photoemission of molecule  $\mathcal{A}$  occurs with no effective nuclear motion, i.e., the electron and nuclear degrees of freedom  $x$  and  $R$ , respectively, are *de facto* uncoupled due to the relative positions of the ground state and ionic curves [see Fig. 1(a)].

We now move on to the results obtained with the  $\mathcal{B}$  and  $\mathcal{C}$  molecules, for which photoemission occurs along with sensible nuclear dynamics.

#### IV. PHOTOEMISSION FROM MOLECULES $\mathcal{B}$ AND $\mathcal{C}$ : SIGNATURES OF THE VIBRONIC COUPLINGS

The necessity of taking the nuclear motion into consideration in near-threshold photoemission from molecules  $\mathcal{B}$  and  $\mathcal{C}$  is a consequence of the relative position shifts of their ground states and ionic BO curves [see Figs. 1(b) and 1(c)]. We investigate how it affects the photoemission dynamics in the present section by presenting and analyzing the orientation-resolved photoemission yields and stereo delays in these two model molecules and addressing the relevance of fixed-nuclei simulations in this context.

##### A. Complete simulations

We use here the same pulse parameters as in the simulations with molecule  $\mathcal{A}$  (Sec. III A).

##### 1. Signatures of electron-nucleus couplings

A striking signature of the electron-nuclei couplings in the photoemission dynamics of  $\mathcal{B}$  shows up in the delays inferred from the outgoing flux. In contrast to the previous case, the stereo delays measured according to Eqs. (10) and (11) strongly depend on the detection distance  $r_d$ . This is illustrated in Table I with a few representative cases. Not only does it evidence a rather dramatic dependence of  $\Delta\tau$  with respect to  $r_d$ , well above the numerical accuracy of the simulations, but it turns out that  $\Delta\tau$  monotonically diverges with increasing  $r_d$

TABLE I. Stereo delay  $\Delta\tau$  computed according to Eq. (11) in molecule  $\mathcal{B}$  for an illustrative set of detection distances  $r_d$  and photon frequencies  $\omega_{XUV}$ .

$\omega_{XUV}$ (eV)	$r_d$ (a.u.)	$\Delta\tau$ (as)
32.6	600	119
32.6	800	153
34.1	800	74
34.1	1000	89

(not shown). This tells us that the delays computed as such are irrelevant for an objective characterization of the ionization dynamics.

Nevertheless, the dependence on  $r_d$  bears crucial information: It suggests that the electron wave packets travel on each side of the molecule with slightly different average velocities. This is the signature of an anisotropic momentum sharing between the nuclei and the active electron during the *concerted* ionization and contraction of the molecular ion. It involves the nuclear mass asymmetry since the lighter the nucleus is, the more the photoelectron is prone to share kinetic energy with it. The principle, which applies to the average velocity, is sketched in Fig. 5. Assuming that only the lighter nucleus (on the left) significantly moves, the photoelectron ends up with a lower velocity if it exits in the direction of motion of that nucleus (towards the right) than in the other direction. Properly accounting for this momentum sharing hence requires giving up global characterization and rather considering vibrationally resolved observables. In the present context, they are derived from the channel-resolved wave packets

$$\varphi_v(x, t) = \int_0^\infty \chi_v(R)\Phi(x, R, t)dR \quad (17)$$

in the vibronic TDSE simulations. In Eq. (17),  $\chi_v(R)$  are the vibrational eigenstates of the molecular ionic core Hamiltonian  $H_N$  [see Eq. (1) and the Appendix]. The individual channel functions are relevant as soon as they are uncoupled from each other, i.e., in the asymptotic  $x$  region where  $V_{N-e}$  no longer depends significantly on  $R$  (typically beyond a few hundred a.u.). Each channel is assigned a specific ionization

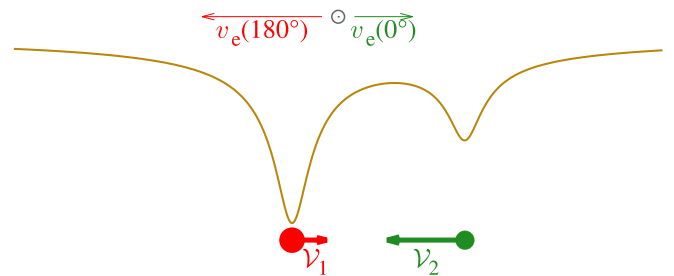


FIG. 5. Sketch of the asymmetric average momentum sharing between the photoelectron (open circle) and the nuclei (closed circles) during the concerted photoionization and early contraction of molecule  $\mathcal{B}$ . For the sake of clarity, the velocity asymmetries have been exaggerated compared to the ones obtained in the actual simulations.

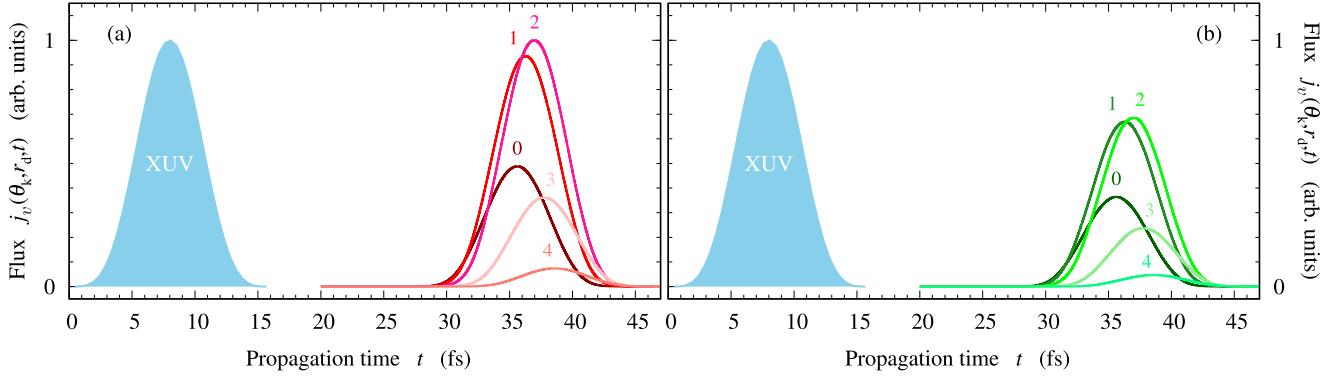


FIG. 6. Vibrationally resolved outgoing electron flux  $j_v(\theta_k, r_d, t)$  computed, in the fully correlated simulations, at  $r_d = 800$  a.u. on the (a) left ( $\theta_k = 180^\circ$ ) and (b) right ( $\theta_k = 0^\circ$ ) sides of molecule  $\mathcal{B}$  ionized by an  $\omega_{\text{XUV}} = 35.67$  eV pulse, as a function of propagation time  $t$ , for the first five dominant channels. Each curve is labeled according to its corresponding channel ( $v = 0-4$ ). The flux is normalized to 1 at the overall maximum reached in the  $v = 2$  channel, on the left side. The temporal envelope of the ionizing pulse is represented by the blue filled curve.

potential

$$E_1(v) = \mathcal{E}_v^{(+)} - \mathcal{E}_0^{(0)}, \quad (18)$$

where  $\mathcal{E}_v^{(+)}$  is the energy of the corresponding ionization threshold (in the BO framework, that is the eigenvalue of  $H_N$  associated with  $\chi_v$ ) and  $\mathcal{E}_0^{(0)}$  the vibronic ground energy of the neutral molecule.

The key time-dependent observable becomes the *vibrationally resolved* electron flux

$$j_v(\theta_k, r_d, t) = \cos \theta_k \text{Im}[\varphi_v^*(r_d \cos \theta_k, t) \varphi_v'(r_d \cos \theta_k, t)]$$

computed at a distance  $r_d$  on each side of the molecule. Vibrationally resolved anisotropic yields and delays can be computed from the flux  $j_v(\theta_k, r_d, t)$  in a similar fashion to the integrated case (see Sec. III).

The flux computed at the distance  $r_d = 800$  a.u. on the left and right sides of the  $\mathcal{B}$  molecule submitted to an  $\omega_{\text{XUV}} = 35.67$  eV pulse is shown in Figs. 6(a) and 6(b), respectively, for the first few populated channels. The flux maxima of the different channels are time shifted from each other, which is a manifestation of the energy conservation law

$$\varepsilon = \omega_{\text{XUV}} - E_1(v). \quad (19)$$

The larger the  $E_1(v)$ , the lower the photoelectron energy  $\varepsilon$  and the longer the time needed to reach the detector. As for molecule  $\mathcal{A}$ , the asymmetry of molecule  $\mathcal{B}$  results in anisotropic ionization yields, visible when comparing the flux magnitudes on the left and on the right. Similar results were obtained with molecule  $\mathcal{C}$  (not shown).

To get better insight into the vibrational distributions upon ionization, we display in Figs. 7(a) and 7(b), column i, the Franck-Condon (FC) factors for molecules  $\mathcal{B}$  and  $\mathcal{C}$ , respectively, defined as

$$F(v) = \left| \int_0^\infty \chi_v(R) \xi_0(R) dR \right|^2, \quad (20)$$

where  $\xi_0(R)$  is the ground vibrational wave function of the neutral molecule treated in the BO framework. The FC factors peak at  $v = 1$  for both model molecules and extend significantly up to  $v = 4$  and 8 for molecules  $\mathcal{B}$  and  $\mathcal{C}$ , respectively.

They qualitatively reproduce the actual  $v$ -resolved yields

$$\mathcal{Y}(v; \theta_k) = \int j_v(\theta_k, r_d, t) dt \quad (21)$$

computed on the left (columns ii) and right (columns iii) sides of the molecules ionized by the illustrative  $\omega_{\text{XUV}} = 35.67$  eV pulse. For the sake of comparison, the displayed data are normalized such that each set sums to 1. A feature that

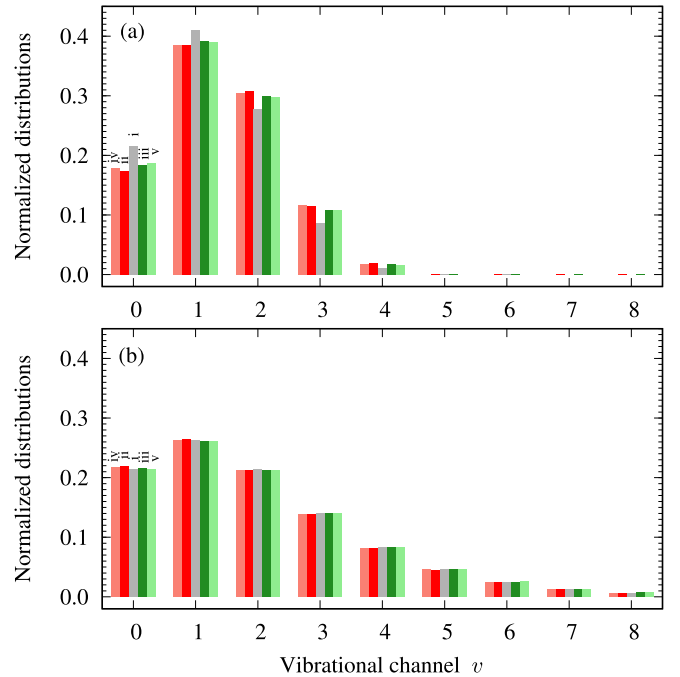


FIG. 7. Vibrational distribution of photoemission from molecules (a)  $\mathcal{B}$  and (b)  $\mathcal{C}$  with an  $\omega_{\text{XUV}} = 35.67$  eV pulse: (i) Franck-Condon factors  $F(v)$  [Eq. (20)]; (ii) and (iii) normalized yields computed in the fully correlated simulations  $\mathcal{Y}(v; 180^\circ)$  and  $\mathcal{Y}(v; 0^\circ)$  [Eq. (21)], respectively; and (iv) and (v) normalized yields computed in the BO framework at the optimal internuclear distances  $R_{\text{opt}}(v)$  and  $\tilde{\mathcal{Y}}(v; 180^\circ)$  and  $\tilde{\mathcal{Y}}(v; 0^\circ)$  [Eq. (25)], respectively. The displayed data are normalized such that each set sums up to 1, for comparison.

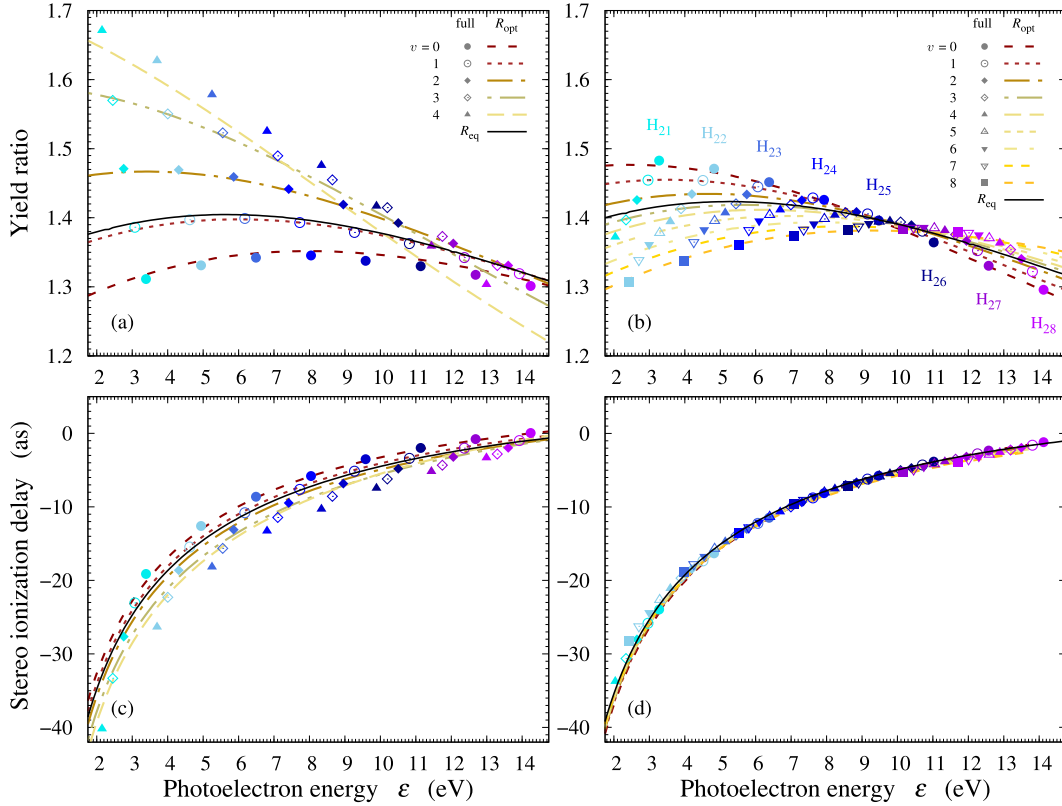


FIG. 8. Vibrationally resolved anisotropic photoemission from molecules (a) and (c)  $\mathcal{B}$  and (b) and (d)  $\mathcal{C}$ . All data are plotted as a function of the photoelectron energy  $\varepsilon$ . (a) and (b) Left-right yield ratio computed in the fully correlated simulations and in the BO framework,  $\mathcal{R}(v)$  (symbols) and  $\tilde{\mathcal{R}}(v)$  (lines), respectively. (c) and (d) Stereo delays computed in the fully correlated simulations and in the BO framework,  $\Delta\tau(v)$  (symbols) and  $\Delta\tau_w(v)$  (lines), respectively. In all frames, the data are displayed for the first few significant vibrational channels; see the legends for details. The displayed BO data were computed at a set of  $v$ -dependent optimal distances  $R_{\text{opt}}(v)$  for molecule  $\mathcal{B}$  and at a set of vertical distances  $R_{\text{vrt}}(v)$  for molecule  $\mathcal{C}$  (for details see the text and Table II). The BO data computed at the equilibrium distance  $R_{\text{eq}}$  are also shown for both molecules.

cannot be included in the FC factors alone is obviously the orientation dependence. In particular for molecule  $\mathcal{B}$ , the vibrational distributions of the yields in Fig. 7(a) display slight yet significant differences on the left and right emission sides. In spite of being small, these discrepancies are sufficient to result in different average photoelectron velocities and to the above-mentioned  $r_d$  dependence of the *integrated* left-right delay  $\Delta\tau$ . We emphasize that the data in Fig. 7 are normalized to highlight the orientation-resolved vibrational distributions and therefore discard the vibrationally resolved absolute magnitude of the ionization probability on each side of the molecules.

## 2. Photoemission yields and delays

Further insight into the  $v$ -resolved photoemission anisotropy is provided in Figs. 8(a) and 8(b), which show, for molecules  $\mathcal{B}$  and  $\mathcal{C}$ , respectively, the yield ratio

$$\mathcal{R}(v) = \frac{\mathcal{Y}(v; 180^\circ)}{\mathcal{Y}(v; 0^\circ)} \quad (22)$$

obtained with several values of  $\omega_{\text{XUV}}$  in the complete simulations (symbols), as a function of the photoelectron energy  $\varepsilon$ . Their values, comprised between approximately 1.2 and approximately 1.7, follow for each  $v$  the global trend observed

with molecule  $\mathcal{A}$  [see Fig. 3(a)]; however, they display a clear additional  $v$  dependence for both molecules  $\mathcal{B}$  and  $\mathcal{C}$ .

We characterize the dynamics revealed in these simulations consistently with the unresolved case [see Eq. (11)]. Here the channel-resolved stereo delays are defined as

$$\Delta\tau(v) = \tau(v; 180^\circ) - \tau(v; 0^\circ) - 2 \frac{\langle x \rangle_0}{\sqrt{2\varepsilon}}, \quad (23)$$

where the numerical TOF towards the virtual detector

$$\tau(v; \theta_k) = \frac{\int t j_v(\theta_k, r_d, t) dt}{\int j_v(\theta_k, r_d, t) dt} \quad (24)$$

is now computed in each  $v$  channel. In Eq. (23), one should keep in mind that  $\varepsilon$  implicitly depends on  $v$  through Eq. (19), for a given  $\omega_{\text{XUV}}$ . We have notably checked that the *vibrationally resolved* stereo delays  $\Delta\tau(v)$  do not depend on  $r_d$ , in contrast with the *v integrated* data discussed before for molecule  $\mathcal{B}$  (Table I). Indeed, for each vibrational channel, energy conservation ensures a symmetric asymptotic electron velocity. The obtained  $v$ -dependent stereo delays are plotted as symbols in Figs. 8(c) and 8(d) for molecules  $\mathcal{B}$  and  $\mathcal{C}$ , respectively. We first note that they globally behave like the stereo delays reported for molecule  $\mathcal{A}$  in Fig. 3(b), with a comparable order of magnitude which decays smoothly towards



TABLE II. Channel-dependent ionization energy  $E_I$  [Eq. (18)], representative internuclear distances  $R_{\text{vrt}}$ , and  $R_{\text{opt}}$  [for details see the text and Eq. (26)] for molecules  $\mathcal{B}$  and  $\mathcal{C}$  in the main vibrational ionization channels  $v$ .

$v$	(a) Molecule $\mathcal{B}$					(b) Molecule $\mathcal{C}$								
	0	1	2	3	4	0	1	2	3	4	5	6	7	8
$E_I$ (eV)	29.17	29.48	29.78	30.10	30.41	29.30	29.61	29.92	30.23	30.53	30.83	31.13	31.42	31.71
$R_{\text{vrt}}$ (Å)	1.076	1.106	1.145	1.201	1.319	1.160	1.135	1.115	1.098	1.082	1.066	1.055	1.041	1.031
$R_{\text{opt}}$ (Å)	1.084	1.113	1.146	1.203	1.248	1.174	1.148	1.124	1.105	1.091	1.079	1.069	1.055	1.038

0 when the photoelectron energy  $\varepsilon$  increases. In addition, a marked  $v$  dependence is observed in molecule  $\mathcal{B}$ , reminiscent of the behavior of the corresponding yield ratios [Fig. 8(a)]. In molecule  $\mathcal{C}$ , however, the values of  $\Delta\tau(v)$  appear to depend mostly on  $\varepsilon$  regardless of the vibrational channel, since all of them follow a common spectral evolution. This is consistent with the normalized vibrational distributions displayed in Fig. 7(b), which are almost identical in the two directions, as pointed out before.

### B. Simulations at fixed internuclear distances

In this section we investigate the possibility of retrieving the orientation-dependent data, including their  $v$  dependences, by analyzing electronic continuum wave functions obtained in simulations with fixed nuclei.

The yield ratio and delays computed for both molecules in the BO framework at  $R_{\text{eq}}$  according to Eq. (14) are displayed as a black solid lines in Fig. 8. They lie near the data obtained for the dominant channels in the full TDSE simulations (between  $v = 1$  and 2) and very close to the equivalent results obtained with  $\mathcal{A}$  [see Fig. 3(a)]. Nevertheless, and quite obviously, simulations performed at a *single* fixed internuclear distance cannot reproduce the nontrivial  $v$  dependence observed in the full simulations for the yield ratio and stereo delays of molecule  $\mathcal{B}$  and for the yield ratio of molecule  $\mathcal{C}$ .

Below we use the simulations performed on molecule  $\mathcal{B}$  to identify and interpret  $v$ -dependent geometries that allow us to reproduce the results of the vibronic simulations with the fixed-nuclei approach. We then assess our interpretation by applying it to fixed-nuclei simulations on molecule  $\mathcal{C}$ .

#### 1. Optimal conformations for molecule $\mathcal{B}$

By scanning through the support of the initial vibrational state  $\xi_0(R)$  of molecule  $\mathcal{B}$  ( $R \sim 1.0$ – $1.3$  Å), we identified empirically a set of channel-specific optimal distances  $R_{\text{opt}}(v)$  for which both the yield ratio and the stereo delays in the BO approach reproduce the ones of the complete vibronic simulations. The values of  $R_{\text{opt}}(v)$  obtained are reported in Table II(a). The orientation- and channel-resolved yields, now computed in the BO framework at a given optimal conformation for each channel,

$$\tilde{\mathcal{Y}}(v; \theta_k) = |A(R_{\text{opt}}(v); \theta_k)|^2 F(v), \quad (25)$$

are displayed for the left and right sides in columns iv and v of Fig. 7(a), respectively. They reproduce very well the asymmetric  $v$  dependence of the actual yields  $\mathcal{Y}(v; \theta_k)$  (columns ii and iii). The corresponding yield ratio  $\tilde{R}(v)$  and stereo delays  $\Delta\tau_w(v)$ , extracted from the SCWF computed at the

optimal conformation for each  $v$ , are displayed as solid lines in Figs. 8(a) and 8(c). They are in excellent agreement with the  $v$ -dependent data obtained in the fully correlated simulations for both molecules, apart from  $v = 4$ , as will be discussed below.

#### 2. Physical interpretation

The optimal molecular conformations can be interpreted by looking at the  $R$ -dependent ionization potential  $\tilde{E}_I(R)$  [Eq. (4)], which for molecule  $\mathcal{B}$  increases monotonically with  $R$  within the support of  $\xi_0(R)$  [see Fig. 9(a)]. In the same figure we indicate the internuclear distances  $R_{\text{vrt}}(v)$  at which  $\tilde{E}_I$  matches the  $v$ -dependent ionization potential [Eq. (18)],

$$\tilde{E}_I[R_{\text{vrt}}(v)] = E_I(v). \quad (26)$$

These vertical internuclear distances are reported in Table II(a) for comparison with the optimal distances found empirically. It turns out that  $R_{\text{opt}}$  matches  $R_{\text{vrt}}$  within approximately 1% in all the considered channels, except  $v = 4$  (approximately 5%).

Alternative insight from the wave function perspective can be gained by expressing the channel-resolved photoemission probability as

$$d_v(\theta_k) = \int \tilde{d}(R; \theta_k) O_v(R) dR, \quad (27)$$

where  $\tilde{d}(R; \theta_k)$  is the orientation-resolved electronic dipole computed at each  $R$  and  $O_v(R) = \chi_v(R)\xi_0(R)$  is the nuclear overlap function introduced in Eq. (20). Our approach consists in approximating the  $R$  integration as  $d_v(\theta_k) \approx \tilde{d}(R_{\text{opt}}(v); \theta_k) O_v[R_{\text{opt}}(v)]$ . We found that in each channel but  $v = 4$ , both  $R_{\text{opt}}$  and  $R_{\text{vrt}}$  lie in the vicinity of  $R_{\text{ctp}}$ , the ionic classical turning point nearest  $R_{\text{eq}}$  (see the Appendix). In essence, this turning point approximately fulfills Eq. (26) within or near the FC region, i.e., in the main open channels. Here  $R_{\text{opt}}(v) \approx R_{\text{ctp}}(v)$  and therefore it appears as a characteristic distance for the vibrational wave function  $\chi_v(R)$  within the support of the initial state  $\xi_0(R)$  while the  $v$ -independent dipole smoothly evolves with  $R$ . [See Ref. [56] for a full treatment, articulated around Eq. (27), of anisotropic photoemission with vibrational resolution.]

We repeated the same procedure for molecule  $\mathcal{C}$ . The optimal internuclear distances  $R_{\text{opt}}(v)$  that we found empirically are reported in Table II(b), together with the vertical ones  $R_{\text{vrt}}(v)$  extracted from the ionization potential displayed in Fig. 9(b). Here also  $\tilde{E}_I(R)$  is a monotonic function of  $R$ , with opposite variations than for molecule  $\mathcal{B}$  (as mentioned earlier, molecule  $\mathcal{B}$  contracts upon ionization, while molecule

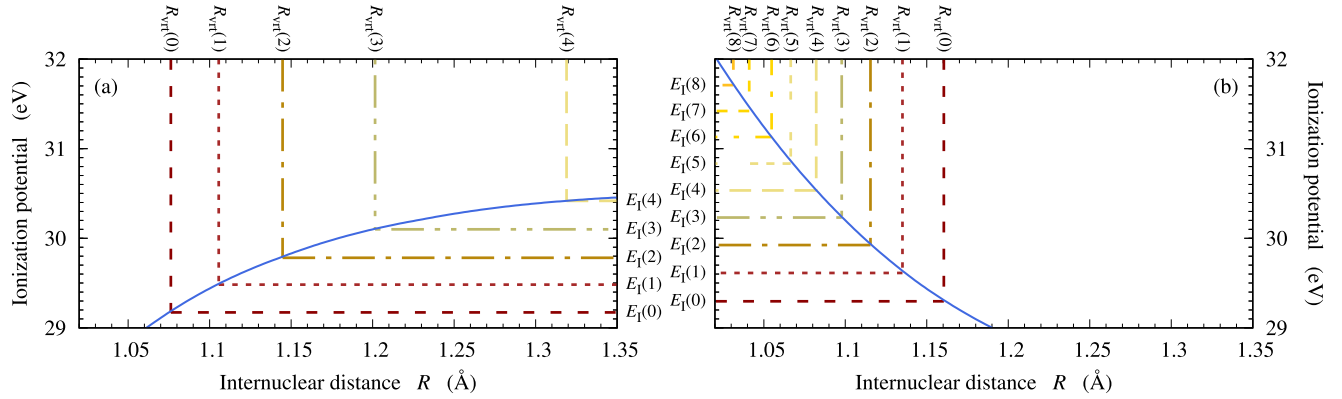


FIG. 9. Vertical ionization potential  $\tilde{E}_1(R)$  of molecules (a)  $\mathcal{B}$  and (b)  $\mathcal{C}$  as a function of  $R$  (blue solid curve), used to identify the internuclear distances  $R_{\text{vrt}}(v)$  fulfilling Eq. (26) out of the  $v$ -dependent ionization potentials  $E_1(v)$ .

$\mathcal{C}$  expands upon ionization). For this molecule, very good agreement is found between  $R_{\text{opt}}(v)$ ,  $R_{\text{vrt}}(v)$ , and  $R_{\text{ctp}}(v)$  in all open channels (see the Appendix). The BO data displayed as lines in Figs. 8(b) and 8(d) for molecule  $\mathcal{C}$  were directly obtained with  $R_{\text{vrt}}(v)$ . The differences from the data obtained using  $R_{\text{opt}}(v)$  (not shown) would be hardly discernible in that figure. The agreement between the complete simulations and the fixed-nuclei approach is excellent here in all considered channels, including the ionization ratios [Fig. 8(b)] which follow spectral trends that significantly depend on  $v$ .

These results provide a simple physical criterion for selecting *a priori* a set of optimal conformations which allow reproducing, in a fixed-nuclei framework, the details of  $v$ -dependent molecular photoionization dynamics. It is nevertheless likely that these specific distances can be representative of the  $v$ -dependent photoemission dynamics only when  $\tilde{E}_1(R)$  varies monotonically with  $R$ . In particular, for molecule  $\mathcal{B}$  the  $\tilde{E}_1(R)$  variations are less pronounced as  $R$  grows towards the  $R_{\text{vrt}}$  of the highest channels, within the studied range. Consistently, the data computed in the BO framework for molecule  $\mathcal{B}$  turned out to be less sensitive to small  $R$  variations beyond  $R_{\text{opt}}(v=3)$ , to the extent that we could not find an optimal distance for the  $v=4$  channel with the same accuracy as for other channels. This is particularly visible in the yield ratio [Fig. 8(a)], where the BO data never reach the “exact” ones obtained for the highest ( $v=4$ ) channel, the displayed BO data corresponding to  $R_{\text{opt}}(v=4)$  being the closest one could get. This however concerns a minor channel [see Fig. 7(a)]. For molecule  $\mathcal{C}$ , the narrower distributions of the data can be directly related to the sharper monotonic decay of  $\tilde{E}_1$  when  $R$  increases, which implies a narrower dispersion of  $R_{\text{vrt}}(v)$  than for molecule  $\mathcal{B}$ .

### C. Illustrative applications of the optimal conformations

In this section we address the relevance of the optimal conformations beyond the context in which they were identified. We investigate their relevance first in simulations of interferometric RABBIT measurements and then to include electron-ion coherences during broadband one-photon ionization.

The RABBIT scheme, together with the attosecond streaking approach, provides indirect ways to access photoemission

dynamics,<sup>2</sup> the direct time domain approaches used in our simulations having no experimental equivalent with attosecond resolution, e.g., magnetic bottles have typical dead times of a few tens of nanoseconds [57] and time-to-digit converter resolutions in the 100-ps range [58].

These are interferometric techniques where the time domain information is extracted from the spectral variations of measured phases. Coherence is thus an essential issue in the design and exploitation of these approaches, the purpose of which is to reveal the fundamental dynamics of essentially quantum processes.

#### 1. Intrachannel coherences: RABBIT interferometry

Following a standard 800-nm RABBIT scheme [8,14], we simulated photoemission from the three model molecules in the presence of the fundamental IR field and a comb of its odd harmonics  $H_q$  in the XUV domain (orders  $q$  from 21 to 29), with an adjustable pump-probe delay  $\tau_{\text{XUV-IR}}$ . We computed vibrationally and orientationally resolved photoelectron spectra

$$\sigma(v; \varepsilon, \theta_k) = |a(v; \varepsilon, \theta_k)|^2 \quad (28)$$

out of the final amplitudes corresponding to the ionized molecule,  $a(v; \varepsilon, \theta_k)$ . The latter were obtained in the time-dependent simulations through a position-to-momentum Fourier transform of the channel wave packets  $\varphi_v(x, t)$  accumulated in the asymptotic region at each time  $t$  of the propagation (see Appendix C of [59]).

As expected, we obtained sideband (SB) peaks (orders 22–28) resulting from two-photon XUV plus or minus IR transitions, the intensities of which oscillate when  $\tau_{\text{XUV-IR}}$  is tuned [60]. We used long enough pulses (80 fs for the XUV and for the IR) to resolve the vibrational channels in each sideband. This is illustrated in Fig. 10, which shows the vibrationally structured, orientation- and delay-dependent  $\text{SB}_{24}$  obtained with molecule  $\mathcal{B}$ . Similarly to the one-photon case, the relative

<sup>2</sup>See [27] and references therein for discussions dedicated to the links between RABBIT measurements and fundamental photoemission delays.

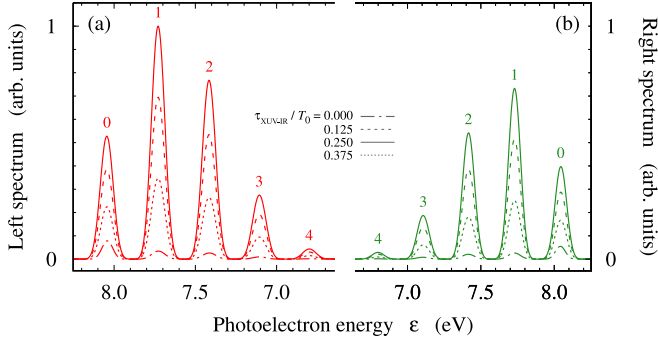


FIG. 10. Photoelectron spectra recorded in RABBIT simulations, on the (a) left and (b) right sides of molecule  $\mathcal{B}$ . The spectral range is focused on sideband 24 and each peak is associated with a specific ionization channel  $v = 0-4$  (see the labels). The different spectra were obtained with different values of the pump-probe delay  $\tau_{\text{XUV-IR}}$  (see the legend, where  $T_0 = 2\pi/\omega_0$  is the laser period).

peak intensities evidence a significantly higher photoemission probability towards the left [Fig. 10(a)] than towards the right [Fig. 10(b)]. Note, however, that the orientation dependence of the SB oscillations are too subtle to be resolved visually in this figure. This is consistent with the ultrashort timescale of the simulated nonresonant photoemission processes [27].

We thus performed an RABBIT analysis consisting in fitting the generic function [60]

$$f(\tau_{\text{XUV-IR}}) = \alpha + \beta \cos(2\omega_0\tau_{\text{XUV-IR}} - \phi) \quad (29)$$

to the  $\tau_{\text{XUV-IR}}$  evolution of each sideband peak associated with a given vibrational channel  $v$  and a given direction  $\theta_k$ . The fitting procedure gives access to the orientation- and channel-resolved phases of the peak oscillations  $\vartheta(v; \theta_k) = \phi$ , as well as to the  $\tau_{\text{XUV-IR}}$ -averaged photoelectron yields  $P(v; \theta_k) = \alpha$ . Since the XUV components in our simulations were all synchronized, i.e., they carry no attochirp,  $\vartheta(v; \theta_k)$  directly corresponds to the so-called molecular phase (see [27] and references therein).

We performed simulations both in the fully correlated approach and in the BO framework. The main results are shown in Fig. 11 for SB<sub>22</sub> to SB<sub>28</sub> in molecules  $\mathcal{A}$  [Figs. 11(a) and 11(d)],  $\mathcal{B}$  [Figs. 11(b) and 11(e)], and  $\mathcal{C}$  [Figs. 11(c) and 11(f)]. The disconnected symbols in the top and bottom frames correspond to the ratio of the  $\tau_{\text{XUV-IR}}$ -averaged yields

$$\mathcal{R}_{\text{RAB}}(v) = \frac{P(v; 180^\circ)}{P(v; 0^\circ)} \quad (30)$$

and the stereo molecular delay [12,19]

$$\Delta\tau_{\text{mol}}(v) = \frac{\vartheta(v; 180^\circ)}{2\omega_0} - \frac{\vartheta(v; 0^\circ)}{2\omega_0}, \quad (31)$$

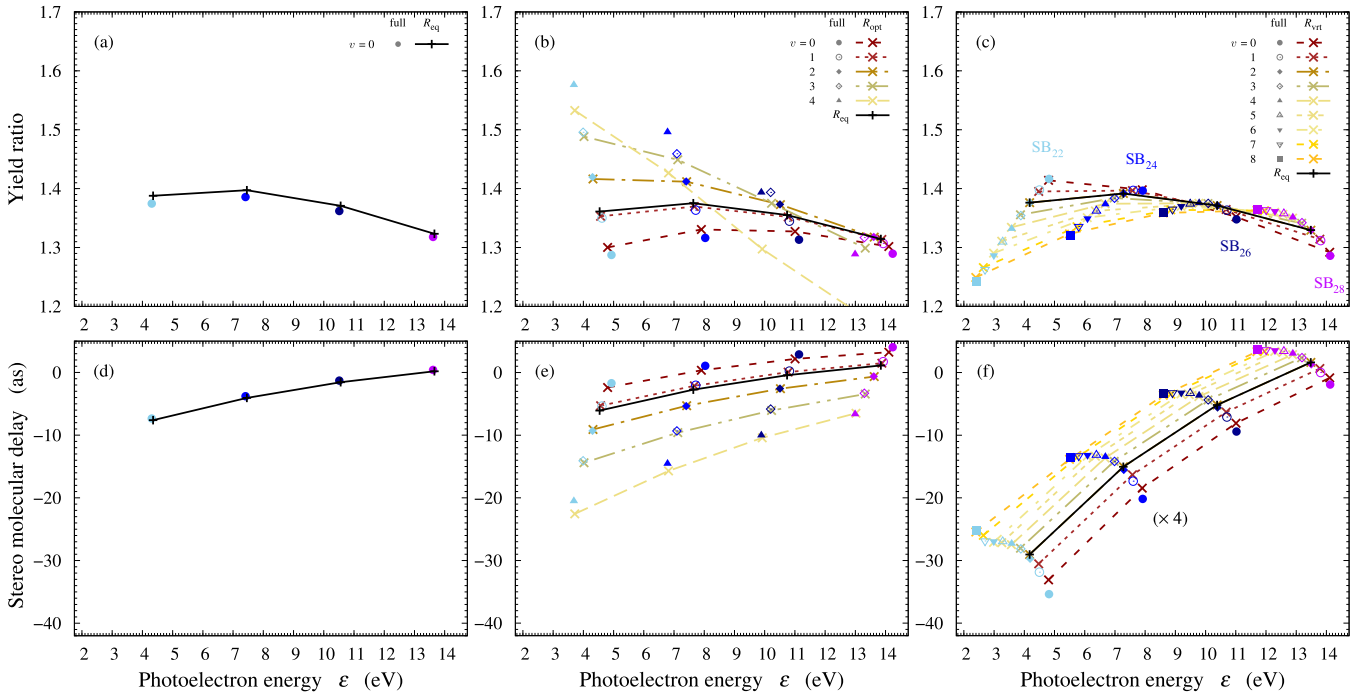


FIG. 11. Simulations of vibrationally resolved anisotropic RABBIT in molecules (a) and (d)  $\mathcal{A}$ , (b) and (e)  $\mathcal{B}$ , and (c) and (f)  $\mathcal{C}$ . Data derived from the analysis of sidebands 22–28 (left to right) are plotted as a function of the photoelectron energy  $\epsilon$ . (a)–(c) Left-right yield ratio computed in the fully correlated simulations and in the BO framework,  $\mathcal{R}_{\text{RAB}}(v)$  (symbols) and  $\tilde{\mathcal{R}}_{\text{RAB}}(v)$  (lines with crosses), respectively. (d)–(f) Stereo molecular delays computed in the fully correlated simulations and in the BO framework,  $\Delta\tau_{\text{mol}}(v)$  (symbols) and  $\tilde{\Delta}\tau_{\text{mol}}(v)$  (lines with crosses), respectively. In each frame, the data are displayed for the first few significant vibrational channels; see the legends for details. Consistently with the results shown in Fig. 8, the displayed BO data were obtained with the set of  $v$ -dependent optimal distances  $R_{\text{opt}}(v)$  identified in one-photon simulations for molecule  $\mathcal{B}$  and the set of vertical distances  $R_{\text{vt}}(v)$  for molecule  $\mathcal{C}$  (for details see the text and Table II). The BO data computed at the equilibrium distance  $R_{\text{eq}}$  are also shown for both molecules. The data displayed in (f) are all multiplied by 4 for better readability.

respectively, obtained in the fully correlated approach for the main  $v$  channels. As in the one-photon case, these quantities follow standard general trends which can be summarized by looking at the single-channel results of molecule  $\mathcal{A}$ . Its yield ratio  $\mathcal{R}_{\text{RAB}}(0)$  decays slowly, from approximately 1.4 down to approximately 1.3 over the covered energy range, which is reminiscent of the one-photon counterpart shown in Fig. 3(a). The stereo molecular delay  $\Delta\tau_{\text{mol}}(0)$  decays in magnitude, from  $-10$  as at  $\text{SB}_{22}$  down to near 0 as at  $\text{SB}_{28}$ . The relationship between the latter and the one-photon ionization delay is the subject of the companion paper [27] and will not be further discussed here. Beyond the trends mentioned above, the results for molecules  $\mathcal{B}$  and  $\mathcal{C}$  display clear  $v$  dependences, both in the yield ratios and in the stereo molecular delays, that are slightly more pronounced than in the one-photon case.

The lines with crosses correspond to the equivalent quantities  $\tilde{\mathcal{R}}_{\text{RAB}}(v)$  and  $\Delta\tilde{\tau}_{\text{mol}}(v)$ , respectively, obtained in time-dependent simulations at *fixed* internuclear distances. For molecule  $\mathcal{A}$ , we used again the equilibrium distance  $R_{\text{eq}}$ , which unsurprisingly perfectly reproduces the results of the complete simulations. Note that these fixed-nuclei data appear in Fig. 6 of [27]. For molecule  $\mathcal{B}$ , we additionally show the BO results obtained with the  $v$ -dependent optimal distances  $R_{\text{opt}}$  identified in the one-photon simulations (see Table II), while for molecule  $\mathcal{C}$  we used the vertical internuclear distances  $R_{\text{vt}}(v)$ . The data obtained at  $R_{\text{eq}}$  with both molecules  $\mathcal{B}$  and  $\mathcal{C}$  are similar to the ones obtained with molecule  $\mathcal{A}$ . Regarding the results provided at optimal conformations, we clearly see that the BO framework fails to reproduce the yield ratio for molecule  $\mathcal{B}$  in the minority  $v = 4$  channel [Fig. 11(b)], already discussed in the one-photon case. Apart from this, the data obtained in the BO framework, including the stereo molecular delays in all channels for both molecules, are in excellent agreement with the data obtained in the complete simulations. This illustrates the capacities of BO approaches with appropriate internuclear distances to simulate vibrationally resolved RABBIT measurements with high fidelity.

## 2. Interchannel coherences: Broadband photoemission

As our last case, we now highlight the capacities of fixed-nuclei approaches to keep track of *interchannel* coherences when reconstructing the complete vibronic wave packet out of a set of simulations performed at the  $v$ -dependent optimal conformations. To this end, we simulated the photoionization of molecules  $\mathcal{B}$  and  $\mathcal{C}$  with a broad XUV pulse of central frequency  $\omega_{\text{XUV}} = 37.23$  eV ( $H_{24}$  of a 800-nm laser) and a duration of 8 fs (three fundamental IR cycles) in the one-photon perturbative regime. The bandwidth of this pulse overlaps a few vibrational channels in the photoelectron spectra, as shown in Fig. 12 for molecule  $\mathcal{B}$ . We therefore partially lose the vibrational resolution when looking at the  $v$ -integrated spectra, in contrast to the results obtained with narrower pulses (see, for instance, Fig. 10).

From the final channel-selective amplitudes in the continuum  $a(v; \varepsilon, \theta_k)$ , we computed the reduced density matrix

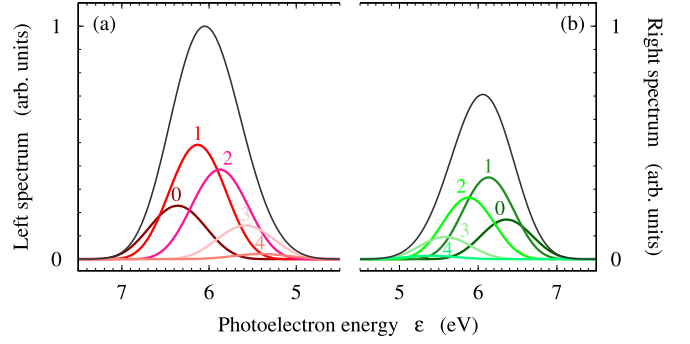


FIG. 12. Photoelectron spectrum recorded on the (a) left and (b) right sides of molecule  $\mathcal{B}$ , upon single-photon ionization with an 8-fs pulse of 37.23 eV central frequency ( $H_{24}$  of a 800-nm field). Thick colored lines show  $v$ -resolved spectra ( $v = 0-4$ ; see the labels) and thin gray lines  $v$ -integrated spectra.

(RDM) of the ion in the final state as

$$\rho_{\text{ion}}(v, v') = \sum_{\theta_k=0^\circ, 180^\circ} \int_{\Delta} d\varepsilon [a(v; \varepsilon, \theta_k)]^* a(v'; \varepsilon, \theta_k), \quad (32)$$

where  $[\ ]^*$  denotes the complex conjugate and the spectral integration range  $\Delta$  is restricted to the overall support of the photoelectron spectrum. The modulus of the RDM computed in the complete simulations for molecules  $\mathcal{B}$  and  $\mathcal{C}$  in the main vibrational channels is shown in Figs. 13(a) and 13(c), respectively. For both molecules, we observe nonvanishing off-diagonal elements which are signatures of coherences between overlapping channels ( $|v' - v| \lesssim 3$ ).

In the fixed-nuclei simulations, we reconstructed the final RDM of the ion out of the amplitudes  $\tilde{a}(R_{\text{opt}}(v); \varepsilon, \theta_k)$  obtained in time-dependent simulations using the  $v$ -dependent vertical internuclear distances  $R_{\text{vt}}(v)$  for both molecules. The results are shown in Figs. 13(b) and 13(d) for molecules  $\mathcal{B}$  and  $\mathcal{C}$ , respectively. The overall agreement with the complete simulations is excellent for both the populations (diagonal elements) and the coherences. To further evaluate the quality of these reconstructed vibrational RDMs, we computed in each simulation the purity of the final state

$$p = \frac{\text{tr}(\rho_{\text{ion}}^2)}{\text{tr}(\rho_{\text{ion}})^2}, \quad (33)$$

where  $\text{tr}(\ )$  denotes the trace operation. The purity values are indicated in Fig. 13 at the top of each matrix.<sup>3</sup> The purity in fixed-nuclei results accurately match the exact ones, within less than 1%, for both molecules. It is worth noting that, when using the  $R_{\text{opt}}(v)$  conformations rather than the  $R_{\text{vt}}(v)$  ones, the fixed-nuclei simulations agree with the exact ones with approximately 10% accuracy only (results not shown).

<sup>3</sup>We verified that the normalized matrices and the purities remain practically unchanged when looking at the  $\theta$ -dependent RDM obtained as in Eq. (32) but without angular integration (results not shown). This is consistent with the weak  $\theta_k$  dependence of the normalized probabilities displayed in Fig. 7.



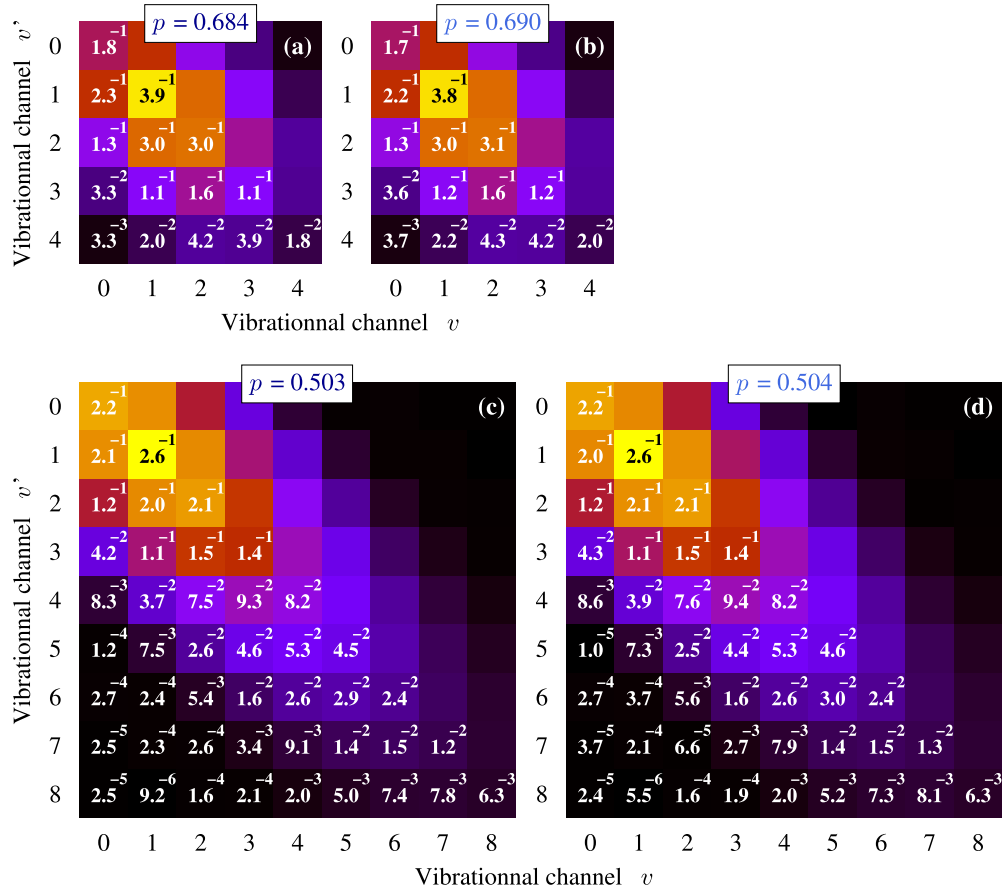


FIG. 13. Photoionization of molecules (a) and (b)  $B$  and (c) and (d)  $C$  with a broadband XUV pulse (same simulations as in Fig. 12). Modulus of the final ion's reduced density matrix  $\rho_{\text{ion}}(v, v')$  [Eq. (32)] computed in (a) and (c) complete simulations and (b) and (d) simulations at fixed conformation  $R_{\text{vib}}(v)$ . The values of the matrix elements' moduli are provided in the lower triangles (where the compact notation  $m^y$  stands for  $m \times 10^y$ ). The matrices are displayed for the main open channels. Each one is normalized to have a trace equal to 1, consistently with the data displayed in Fig. 7. The value of the purity  $p$  [Eq. (33)] is indicated at the top of each matrix.

On the one hand, this underlines the sensitivity of the computed purity with respect to the conformations used in the fixed-nuclei approach. On the other hand, it emphasizes the remarkable efficiency of the combined vertical conformations to reproduce the exact interchannel coherent dynamics.

## V. CONCLUSION

We studied numerically how nuclear motion affects the dynamics of orientation-resolved photoemission in asymmetric diatomic model molecules presenting minimal vibronic couplings. We considered near-threshold photoemission in the absence of any resonance, where the so-called stereo Wigner delays amount to a few tens of attoseconds or less.

We have shown that the intrinsic molecular asymmetry results in an anisotropic electron-ion momentum sharing which, as slight as it may be, may prevent us from assigning unambiguously a stereo Wigner delay to the *channel-averaged* photoemission process. Indeed, a small asymmetry in the average photoelectron energy leads to stereo delay values that diverge when the (virtual) detection distance increases. This is circumvented by considering vibrationally resolved

photoemission. However, on the theory side, comprehensive time-dependent vibronic simulations of molecules interacting with external fields are restricted to smaller molecules such as  $H_2$  with a limited range of physical and numerical parameters or to simplified low-dimensional model molecules such as the ones used in the present work.

Therefore, we investigated ways of retrieving the vibrationally resolved photoemission dynamics revealed by the complete vibronic simulations out of more standard and broadly applicable time-independent approaches with fixed nuclei. We found empirically that each vibrational channel could be assigned an effective internuclear distance that reproduces the channel-resolved orientation-dependent photoemission yields and delays with good accuracy. Furthermore, we identified a physical criterion, relying on the molecule's ionization energies, that allows selecting *a priori* the  $v$ -dependent effective internuclear distances: It corresponds to the distance for which the vertical ionization potential matches the exact channel-dependent ionization potential. Identifying such unique effective molecular conformations is expected to work efficiently as long as the vertical ionization potential varies significantly when the molecular conformation is changed. Retrieving photoemis-

sion dynamics with vibrational resolution out of fixed-nuclei simulation is also expected to work as long as photoemission takes place with little vibronic correlation, typically in smooth continua with sufficiently separated ionic vibrational levels.

Finally, we assessed the relevance of the fixed-nuclei approach beyond the context in which we identified the effective internuclear distances. We first showed that it could be used to accurately simulate anisotropic vibrationally-resolved RABBIT interferometry, in terms of both phase and amplitudes. Then we investigated the fixed-nuclei approach capacities to account for interchannel coherences in broadband photoionization of our model molecules, where the different channels significantly overlap. We showed that the fixed-nuclei approach could satisfactorily reproduce both the ion's reduced density matrix and purity in the final state. This approach is thus of particular interest in modeling attosecond resolved photoemission dynamics in benchmark molecules without the need to resort to full-fledged vibronic approaches [56]. It is a complement to existing approaches tackling the issues of anisotropy in molecular photoemission but where the details of the photoelectron-ion interactions are neglected (see, e.g., [61,62]). It could be applied to simulate attosecond time-resolved interferometry and to highly nonlinear processes such as strong-field ionization [63] or molecular high-order harmonic generation [46,64–67] and to investigate ultrafast decoherence processes in molecules [35,38,44] of crucial importance in attochemistry.

## ACKNOWLEDGMENTS

This research received financial support from the French National Research Agency through Grants No. ANR-15-CE30-0001-CIMBAAD and No. ANR-20-CE30-0007-DECAP.

## APPENDIX: VIBRATIONAL STATES

### 1. Vibrational basis

Figure 14 shows the ionic vibrational wave functions  $\chi_v(R)$  of the main open channels in single-photon ionization of model molecules  $\mathcal{B}$  [Fig. 14(a)] and  $\mathcal{C}$  [Fig. 14(b)]. These states (with additional minor channels) serve as basis functions for the numerical implementation of the TDSE solver in the complete vibronic simulations (see Sec. II B 1). They are also physically relevant states for the study of vibrationally resolved photoemission. The ground vibrational wave functions of the neutral molecules,  $\xi_0(R)$ , are also shown.

### 2. Characteristic internuclear distances

In each channel, the optimal distance  $R_{\text{opt}}$  (see Sec. IV B) is indicated with a solid vertical line. The vertical distance  $R_{\text{vrt}}$  fulfilling Eq. (26) is indicated with a dotted line. Moreover,

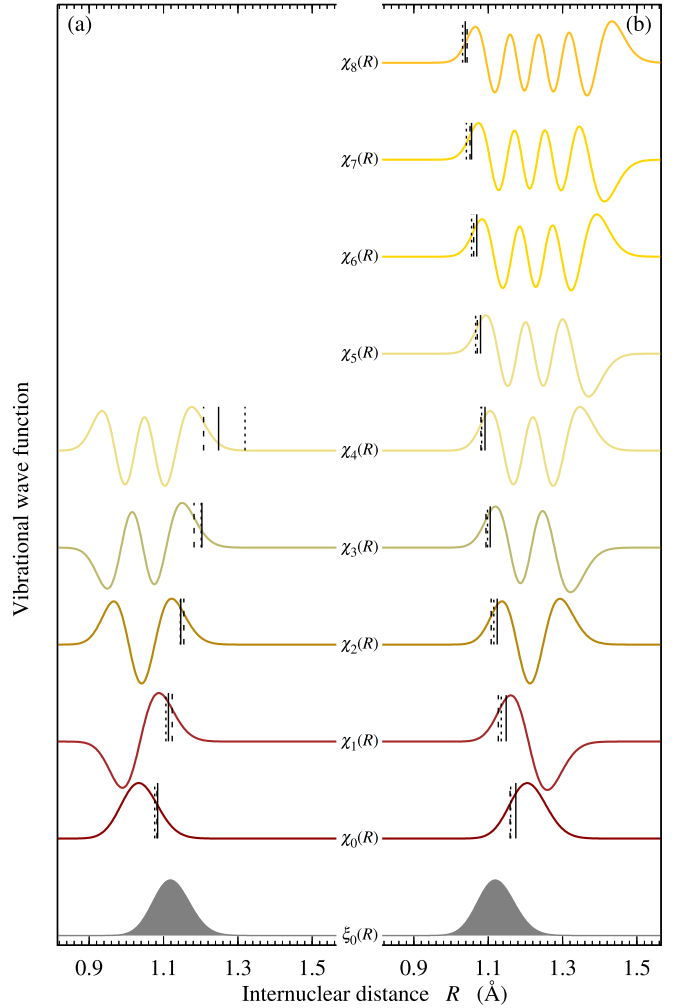


FIG. 14. Final vibrational wave functions  $\chi_v(R)$  in the main ionization channel, as a function of the internuclear distance  $R$ , for model molecules (a)  $\mathcal{B}$  and (b)  $\mathcal{C}$ . The vibrational wave function  $\xi_0(R)$  of the neutral ground state is also shown (see the labels). In each channel, the distances  $R_{\text{opt}}(v)$ ,  $R_{\text{vrt}}(v)$ , and  $R_{\text{ctp}}(v)$  are indicated by a solid line, a dotted line, and a dashed line, respectively.

the distance  $R_{\text{ctp}}(v)$  lying in the FC region and fulfilling

$$V_{\text{N-N}}[R_{\text{ctp}}(v)] = \mathcal{E}_v^{(+)}, \quad (\text{A1})$$

i.e., the classical turning point closest to  $R_{\text{eq}}$ , is indicated with a vertical dashed line. The agreement between the three sets of characteristic distances is very good (except for molecule  $\mathcal{B}$ ,  $v = 4$ , as discussed in the main text).

Given the definitions of  $E_1(v)$  [Eq. (18)] and  $\tilde{E}_1(R)$  [Eq. (4)], on the one hand, and the equations fulfilled by  $R_{\text{vrt}}$  and  $R_{\text{ctp}}$ , respectively, on the other hand, we can expect these two characteristic distances to be nearly equal when the potential energy in the neutral molecule is close to the vibrational ground state  $V_{\text{N-N}}(R) - \tilde{E}_1(R) \approx \mathcal{E}_0^{(0)}$ , corresponding to the FC region. Therefore,  $R_{\text{vrt}} \approx R_{\text{ctp}}$  should apply to the main open ionization channels, as observed empirically in our simulations.

- [1] S. Baker, J. S. Robinson, C. A. Haworth, H. Teng, R. A. Smith, C. C. Chirilă, M. Lein, J. W. G. Tisch, and J. P. Marangos, Probing proton dynamics in molecules on an attosecond time scale, *Science* **312**, 424 (2006).
- [2] P. Salières, A. Maquet, S. Haessler, J. Caillat, and R. Taïeb, Imaging orbitals with attosecond and Ångström resolutions: Toward attochemistry? *Rep. Prog. Phys.* **75**, 062401 (2012).
- [3] F. Lépine, M. Y. Ivanov, and M. J. J. Vrakking, Attosecond molecular dynamics: Fact or fiction? *Nat. Photonics* **8**, 195 (2014).
- [4] S. Bag, S. Chandra, and A. Bhattacharya, Molecular attochemistry in non-polar liquid environments: Ultrafast charge migration dynamics through gold-thiolate and gold-selenolate linkages, *Phys. Chem. Chem. Phys.* **19**, 26679 (2017).
- [5] M. Nisoli, P. Decleva, F. Calegari, A. Palacios, and F. Martín, Attosecond electron dynamics in molecules, *Chem. Rev.* **117**, 10760 (2017).
- [6] I. C. D. Merritt, D. Jacquemin, and M. Vacher, Attochemistry: Is controlling electrons the future of photochemistry? *J. Phys. Chem. Lett.* **12**, 8404 (2021).
- [7] F. Calegari and F. Martín, Open questions in attochemistry, *Commun. Chem.* **6**, 184 (2023).
- [8] P. M. Paul, E. S. Toma, P. Breger, G. Mullot, F. Augé, P. Balcou, H. G. Muller, and P. Agostini, Observation of a train of attosecond pulses from high harmonic generation, *Science* **292**, 1689 (2001).
- [9] M. Hentschel, R. Kienberger, C. Spielmann, G. A. Reider, N. Milosevic, T. Brabec, P. Corkum, U. Heinzmann, M. Drescher, and F. Krausz, Attosecond metrology, *Nature (London)* **414**, 509 (2001).
- [10] A. L. Cavalieri, N. Muller, T. Uphues, V. S. Yakovlev, A. Baltuška, B. Horvath, B. Schmidt, L. Blumel, R. Holzwarth, S. Hendel, M. Drescher, U. Kleineberg, P. M. Echenique, R. Kienberger, F. Krausz, and U. Heinzmann, Attosecond spectroscopy in condensed matter, *Nature (London)* **449**, 1029 (2007).
- [11] M. Schultze, M. Fieß, N. Karpowicz, J. Gagnon, M. Korbman, M. Hofstetter, S. Neppl, A. L. Cavalieri, Y. Komninos, T. Mercouris *et al.*, Delay in photoemission, *Science* **328**, 1658 (2010).
- [12] K. Klünder, J. M. Dahlström, M. Gisselbrecht, T. Fordell, M. Swoboda, D. Guénot, P. Johnsson, J. Caillat, J. Mauritsson, A. Maquet, R. Taïeb, and A. L'Huillier, Probing single-photon ionization on the attosecond time scale, *Phys. Rev. Lett.* **106**, 143002 (2011).
- [13] S. Haessler, B. Fabre, J. Higuette, J. Caillat, T. Ruchon, P. Breger, B. Carré, E. Constant, A. Maquet, E. Mével, P. Salières, R. Taïeb, and Y. Mairesse, Phase-resolved attosecond near-threshold photoionization of molecular nitrogen, *Phys. Rev. A* **80**, 011404(R) (2009).
- [14] H. G. Muller, Reconstruction of attosecond harmonic beating by interference of two-photon transitions, *Appl. Phys. B* **74**, s17 (2002).
- [15] J. Caillat, A. Maquet, S. Haessler, B. Fabre, T. Ruchon, P. Salières, Y. Mairesse, and R. Taïeb, Attosecond resolved electron release in two-color near-threshold photoionization of N<sub>2</sub>, *Phys. Rev. Lett.* **106**, 093002 (2011).
- [16] M. Vacher, R. Gaillac, A. Maquet, R. Taïeb, and J. Caillat, Transition dynamics in two-photon ionisation, *J. Opt.* **19**, 114011 (2017).
- [17] V. J. Borràs, J. González-Vázquez, L. Argenti, and F. Martín, Attosecond photoionization delays in the vicinity of molecular Feshbach resonances, *Sci. Adv.* **9**, eade3855 (2023).
- [18] V. S. Yakovlev, J. Gagnon, N. Karpowicz, and F. Krausz, Attosecond streaking enables the measurement of quantum phase, *Phys. Rev. Lett.* **105**, 073001 (2010).
- [19] A. Chacon, M. Lein, and C. Ruiz, Asymmetry of Wigner's time delay in a small molecule, *Phys. Rev. A* **89**, 053427 (2014).
- [20] J. Vos, L. Cattaneo, S. Patchkovskii, T. Zimmermann, C. Cirelli, M. Lucchini, A. Kheifets, A. S. Landsman, and U. Keller, Orientation-dependent stereo Wigner time delay and electron localization in a small molecule, *Science* **360**, 1326 (2018).
- [21] T. Barillot, C. Cauchy, P.-A. Hervieux, M. Gisselbrecht, S. E. Canton, P. Johnsson, J. Laksman, E. P. Mansson, J. M. Dahlström, M. Magrakvelidze *et al.*, Angular asymmetry and attosecond time delay from the giant plasmon resonance in C<sub>60</sub> photoionization, *Phys. Rev. A* **91**, 033413 (2015).
- [22] P. Hockett, E. Frumker, D. M. Villeneuve, and P. B. Corkum, Time delay in molecular photoionization, *J. Phys. B: At. Mol. Opt. Phys.* **49**, 095602 (2016).
- [23] D. Baykusheva and H. J. Wörner, Theory of attosecond delays in molecular photoionization, *J. Chem. Phys.* **146**, 124306 (2017).
- [24] S. Beaulieu, A. Comby, A. Clergerie, J. Caillat, D. Descamps, N. Dudovich, B. Fabre, R. Géneaux, F. Légaré, S. Petit, B. Pons, G. Porat, T. Ruchon, R. Taïeb, V. Blanchet, and Y. Mairesse, Attosecond-resolved photoionization of chiral molecules, *Science* **358**, 1288 (2017).
- [25] H. Ahmadi, E. Plésiat, M. Moioli, F. Frassetto, L. Poletto, P. Decleva, C. D. Schrötter, T. Pfeifer, R. Moshhammer, A. Palacios, F. Martín, and G. Sansone, Attosecond photoionisation time delays reveal the anisotropy of the molecular potential in the recoil frame, *Nat. Commun.* **13**, 1242 (2022).
- [26] A. Boyer, S. Nandi, and V. Loriot, Attosecond probing of photoionization dynamics from diatomic to many-atom molecules, *Eur. Phys. J. Spec. Top.* **232**, 2001 (2023).
- [27] M. Berkane, A. Desrier, C. Lévêque, R. Taïeb, and J. Caillat, Anisotropic molecular photoemission dynamics: Wigner time delay versus time delay from RABBIT measurements, *Phys. Rev. A* **109**, 013101 (2024).
- [28] S. Patchkovskii, J. Benda, D. Ertel, and D. Busto, Theory of nuclear motion in RABBIT spectra, *Phys. Rev. A* **107**, 043105 (2023).
- [29] M. Kowalewski, K. Bennett, J. R. Rouxel, and S. Mukamel, Monitoring nonadiabatic electron-nuclear dynamics in molecules by attosecond streaking of photoelectrons, *Phys. Rev. Lett.* **117**, 043201 (2016).
- [30] X. Gong, E. Plésiat, A. Palacios, S. Heck, F. Martín, and H. J. Wörner, Attosecond delays between dissociative and non-dissociative ionization of polyatomic molecules, *Nat. Commun.* **14**, 4402 (2023).
- [31] D. Ertel, D. Busto, I. Makos, M. Schmoll, J. Benda, H. Ahmadi, M. Moioli, F. Frassetto, L. Poletto, C. D. Schrötter, T. Pfeifer, R. Moshhammer, Z. Mašín, S. Patchkovskii, and G. Sansone, Influence of nuclear dynamics on molecular attosecond photoelectron interferometry, *Sci. Adv.* **9**, eadh7747 (2023).

- [32] L. Cattaneo, J. Vos, R. Y. Bello, A. Palacios, S. Heuser, L. Pedrelli, M. Lucchini, C. Cirelli, F. Martín, and U. Keller, Attosecond coupled electron and nuclear dynamics in dissociative ionization of  $H_2$ , *Nat. Phys.* **14**, 733 (2018).
- [33] R. Y. Bello, S. E. Canton, D. Jelovina, J. D. Bozek, B. Rude, O. Smirnova, M. Y. Ivanov, A. Palacios, and F. Martín, Reconstruction of the time-dependent electronic wave packet arising from molecular autoionization, *Sci. Adv.* **4**, eaat3962 (2018).
- [34] S. Nandi, E. Plésiat, S. Zhong, A. Palacios, D. Busto, M. Isinger, L. Neoričič, C. L. Arnold, R. J. Squibb, R. Feifel, P. Decleva, A. L'Huillier, F. Martín, and M. Gisselbrecht, Attosecond timing of electron emission from a molecular shape resonance, *Sci. Adv.* **6**, eaba7762 (2020).
- [35] M. J. J. Vrakking, Control of attosecond entanglement and coherence, *Phys. Rev. Lett.* **126**, 113203 (2021).
- [36] A. L. Wang, V. V. Serov, A. Kamalov, P. H. Bucksbaum, A. Kheifets, and J. P. Cryan, Role of nuclear-electronic coupling in attosecond photoionization of  $H_2$ , *Phys. Rev. A* **104**, 063119 (2021).
- [37] Y. Liao, Y. Zhou, L.-W. Pi, Q. Ke, J. Liang, Y. Zhao, M. Li, and P. Lu, Two-center interference and stereo Wigner time delay in photoionization of asymmetric molecules, *Phys. Rev. A* **104**, 013110 (2021).
- [38] M. J. J. Vrakking, Ion-photoelectron entanglement in photoionization with chirped laser pulses, *J. Phys. B: At. Mol. Opt. Phys.* **55**, 134001 (2022).
- [39] X. Gong, W. Jiang, J. Tong, J. Qiang, P. Lu, H. Ni, R. Lucchese, K. Ueda, and J. Wu, Asymmetric attosecond photoionization in molecular shape resonance, *Phys. Rev. X* **12**, 011002 (2022).
- [40] X. Chen, W. Cao, B. Zhan, and P. Lu, Backward scattering impact on the photoionization time delay of asymmetric molecules, *J. Phys. B: At. Mol. Opt. Phys.* **56**, 025602 (2023).
- [41] V. V. Serov and A. S. Kheifets, XUV ionization of the  $H_2$  molecule studied with attosecond angular streaking, *J. Phys. B: At. Mol. Opt. Phys.* **56**, 025601 (2023).
- [42] X. Li, Y. Liu, D. Zhang, L. He, S. Luo, C.-C. Shu, and D. Ding, Visualizing vibrationally resolved attosecond time delay in resonance-enhanced multiphoton ionization of no molecules, *Phys. Rev. A* **108**, 023114 (2023).
- [43] Q. Ke, Y. Zhou, Y. Liao, M. Li, K. Liu, and P. Lu, Spheroidal-wave analysis of time delay in molecular reconstruction of attosecond beating by interference of two-photon transitions around a Cooper-like minimum, *Phys. Rev. A* **108**, 013112 (2023).
- [44] Y. Nabekawa and K. Midorikawa, Analysis of attosecond entanglement and coherence using feasible formulae, *Phys. Rev. Res.* **5**, 033083 (2023).
- [45] J. Caillat, A. Maquet, F. Risoud, and R. Taïeb, Low-dimensional models for simulating attosecond processes in atoms and molecules, in *Attosecond Molecular Dynamics*, edited by M. J. J. Vrakking and F. Lepine (Royal Society of Chemistry, London, 2018), Chap. 2, pp. 38–67.
- [46] M. Lein, Attosecond probing of vibrational dynamics with high-harmonic generation, *Phys. Rev. Lett.* **94**, 053004 (2005).
- [47] K. Houfek, T. N. Rescigno, and C. W. McCurdy, Numerically solvable model for resonant collisions of electrons with diatomic molecules, *Phys. Rev. A* **73**, 032721 (2006).
- [48] P. H. Krupenie and S. Weissman, Potential-energy curves for CO and  $CO^+$ , *J. Chem. Phys.* **43**, 1529 (1965).
- [49] F. A. Gianturco, R. R. Lucchese, and N. Sanna, Calculation of low-energy elastic cross sections for electron- $CF_4$  scattering, *J. Chem. Phys.* **100**, 6464 (1994).
- [50] A. P. P. Natalense and R. R. Lucchese, Cross section and asymmetry parameter calculation for sulfur 1s photoionization of  $SF_6$ , *J. Chem. Phys.* **111**, 5344 (1999).
- [51] M. Huppert, I. Jordan, D. Baykusheva, A. von Conta, and H. J. Wörner, Attosecond delays in molecular photoionization, *Phys. Rev. Lett.* **117**, 093001 (2016).
- [52] A. Chacón and C. Ruiz, Attosecond delay in the molecular photoionization of asymmetric molecules, *Opt. Express* **26**, 4548 (2018).
- [53] R. Gaillac, M. Vacher, A. Maquet, R. Taïeb, and J. Caillat, Attosecond photoemission dynamics encoded in real-valued continuum wave functions, *Phys. Rev. A* **93**, 013410 (2016).
- [54] M. J. Seaton and G. Peach, The determination of phases of wave functions, *Proc. Phys. Soc.* **79**, 1296 (1962).
- [55] E. P. Wigner, Lower limit for the energy derivative of the scattering phase shift, *Phys. Rev.* **98**, 145 (1955).
- [56] O. Kalman, On the vibrational state dependence of the asymmetry parameter of angular distribution in the photoelectron spectra, *Mol. Phys.* **34**, 397 (1977).
- [57] J. Palaudoux, P. Lablanquie, L. Andric, J. H. D. Eland, and F. Penent, Multi-coincidence in cascade Auger decay processes, *J. Phys.: Conf. Ser.* **141**, 012012 (2008).
- [58] F. Penent, D. Cubaynes, P. Lablanquie, J. Palaudoux, S. Guilbaud, O. Moustier, J. Guigand, and J.-M. Bizau, Modification of a cylindrical mirror analyzer for high efficiency photoelectron spectroscopy on ion beams, *Atoms* **8**, 63 (2020).
- [59] J. Caillat, J. Zanghellini, M. Kitzler, O. Koch, W. Kreuzer, and A. Scrinzi, Correlated multielectron systems in strong laser fields: A multiconfiguration time-dependent Hartree-Fock approach, *Phys. Rev. A* **71**, 012712 (2005).
- [60] V. Vénier, R. Taïeb, and A. Maquet, Phase dependence of  $(N + 1)$ -color ( $N > 1$ ) ir-uv photoionization of atoms with higher harmonics, *Phys. Rev. A* **54**, 721 (1996).
- [61] W. Domcke, Vibrational state dependence of the photoelectron angular asymmetry parameter caused by vibronic coupling, *Phys. Scr.* **19**, 11 (1979).
- [62] M. Taylor and G. Worth, in *Ultrafast Photoinduced Processes in Polyatomic Molecules: Electronic Structure, Dynamics and Spectroscopy (Dedicated to Wolfgang Domcke on the Occasion of his 70th Birthday)*, edited by M. F. Gelin, S. Matsika, A. L. Sobolewski, and Y. Tanimura, Vibronic coupling model to calculate the photoelectron spectrum of phenol, special issue of *Chem. Phys.* **515**, 719 (2018).
- [63] N. I. Shvetsov-Shilovski and M. Lein, Transfer learning, alternative approaches, and visualization of a convolutional neural network for retrieval of the internuclear distance in a molecule from photoelectron momentum distributions, *Phys. Rev. A* **107**, 033106 (2023).
- [64] A. Zaïr, T. Siegel, S. Sukiasyan, F. Risoud, L. Brugnera, C. Hutchison, Z. Diveki, T. Auguste, J. W. Tisch, P. Salières, M. Y. Ivanov, and J. P. Marangos, Molecular internal dynamics studied by quantum path interferences in high order harmonic generation, *Chem. Phys.* **414**, 184 (2013).
- [65] F. Risoud, C. Lévêque, M. Labeye, J. Caillat, A. Maquet, P. Salières, R. Taïeb, and T. Shaaran, Laser-induced blurring of



- molecular structure information in high harmonic spectroscopy, [Sci. Rep. 7, 17302 \(2017\)](#).
- [66] B. Zhang and M. Lein, High-order harmonic generation from diatomic molecules in an orthogonally polarized two-color laser field, [Phys. Rev. A 100, 043401 \(2019\)](#).
- [67] M. Labeye, F. Risoud, C. Lévêque, J. Caillat, A. Maquet, T. Shaaran, P. Salières, and R. Taïeb, Dynamical distortions of structural signatures in molecular high-order harmonic spectroscopy, [Phys. Rev. A 99, 013412 \(2019\)](#).